Please cite this article in press as: Sasaki et al., Density functional theory-guided C–C coupling pathways in photocatalytic CO_2 reduction to C_2–C_3 products, Chem Catalysis (2026), https://doi.org/10.1016/j.checat.2026.101846

Chem Catalysis

CellPress

Review

Density functional theory-guided C–C coupling pathways in photocatalytic CO_2 reduction to C_2–C_3 products

Masahito Sasaki,[1,2] Shunya Akano,[1,2] and Yasuo Izumi[1,*]
[1]Department of Chemistry, Graduate School of Science, Chiba University, Yayoi 1-33, Inage-ku, Chiba 263-8522, Japan
[2]These authors contributed equally
*Correspondence: yizumi@faculty.chiba-u.jp
https://doi.org/10.1016/j.checat.2026.101846

THE BIGGER PICTURE Sustainable CO_2 conversion has been intensively investigated worldwide. Among them, photocatalytic conversion of CO_2 into fuels and/or value-added chemical resources is well expected to utilize natural light in a sustainable society. Due to this situation, investigations of photocatalytic CO_2 conversion have been reviewed often, especially since 2010. In clear contrast, the reviews were exclusively based on experiments, and reviews on theoretical studies on photocatalytic CO_2 conversion are rare as far as the authors know. The present review discusses this topic based on density functional theory (DFT) calculations. DFT is a well-utilized theory to support the experimental results and the proposed reaction pathway starting from CO_2 to fuels/resources, especially in reports on photocatalytic CO_2 reduction published later than 2016. Based on the DFT calculations, the rate-determining step is discussed, e.g., hydrogenation of CO_2 to OCOH species on the photocatalyst surface. To determine the rate-determining step, a calculation method to search for the saddle point of reaction step is required, e.g., climbing-image nudged elastic band (CI-NEB) method. A rather simple theoretical approach to search a favorable reaction pathway on the basis of reaction Gibbs energy ($\Delta_r G$) changes has also been widely used in recent studies on photocatalytic CO_2 conversion, especially toward C_{2-3} products, because the C_{2-3} products are more economically viable in sustainable society. The key steps of C–C bond formation are discussed based on either CI-NEB method or $\Delta_r G$ value changes. Finally, further refined methodologies to evaluate the photocatalytic CO_2 reduction pathway, rather than the CI-NEB method, are discussed.

SUMMARY

Photocatalytic CO_2 reduction offers a promising route to fuels and value-added chemicals, with density functional theory (DFT) providing mechanistic insights into the reaction pathways, active sites, and product selectivity. Beyond classical formaldehyde and carbene pathways to CH_4 and CH_3OH, recent studies increasingly target C_2–C_3 products, where C–C bond formation is a critical mechanistic step. This review evaluates proposed C–C coupling pathways, including CO–CO, CO_2–CO_2, CO–CHO, CH_3–CH_3, CO–CHOH, CO–COH, and CHO–CHO coupling, and identifies photocatalyst site characteristics governing multicarbon product formation. Particular emphasis is placed on reaction-pathway calculations using the climbing-image nudged elastic band rather than relying solely on reaction Gibbs energies. Comparisons between DFT predictions and experiments are used to assess plausible active sites and mechanisms. Effects of pH, solvent, and competing H_2 evolution are also discussed, alongside complementary dimer, activation-relaxation technique nouveau (ARTn), and metadynamics approaches.

CLASSICAL HYPOTHESES

CO_2 reduction is an extremely endothermic (or endergonic) reaction, particularly when H_2O is used as the reactant. However, to demonstrate a renewable solution for a sustainable society, predicting favorable reaction pathways is highly desirable, especially toward economically viable products, such as C_2H_4, C_2H_6, C_3H_6, C_3H_8, CH_3OH, and C_2H_5OH. Experimentally, investigating such reaction pathways is challenging because intermediates before the rate-determining step are typically inferred

All rights are reserved, including those for text and data mining, AI training, and similar technologies.

Please cite this article in press as: Sasaki et al., Density functional theory-guided C–C coupling pathways in photocatalytic CO_2 reduction to C_2–C_3 products, Chem Catalysis (2026), https://doi.org/10.1016/j.checat.2026.101846

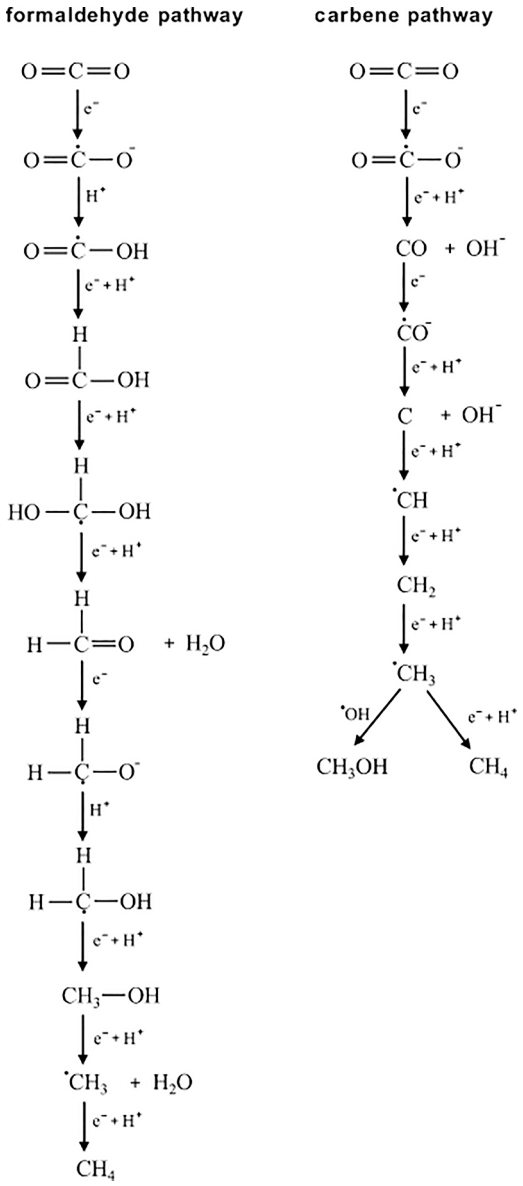

Scheme 1. Two proposed mechanisms for CO_2 reduction: Formaldehyde and carbene pathways

Reprinted with permission from Habisreutinger et al.[4] Copyright 2013 Wiley-VCH.

from reaction kinetics using standard spectroscopy,[1,2] whereas intermediate electron transfer steps are monitored using time-resolved transient spectroscopy.[3]

Density functional theory (DFT) calculations provide a supplementary approach to investigate CO_2 reduction pathways, particularly through techniques for evaluating activation energy (E_{act}) in the elementary reaction step, such as the climbing-image nudged elastic band (CI–NEB) method. This review surveys promising sustainable photocatalytic CO_2 reduction pathways and proposes next steps toward a sustainable society based on DFT calculations. In chapter 1, two classic reaction pathways—formaldehyde (H_2CO) and carbene $(\ddot{C})$—are summarized. The optimization of DFT calculation parameters is briefly summarized in Section S1.

H_2CO pathway

The electrochemical potential for one-electron reduction of CO_2 to CO_2^- is high (−1.90 V versus normal hydrogen electrode at pH 7), demonstrating the difficulty of homogeneous CO_2 transformation[4]:

$$CO_2 + e^- \rightarrow CO_2^-, E^{\ominus} = -1.90\ \text{V}. \quad \text{(Equation 1)}$$

In the classic CO_2 reduction, the "formaldehyde pathway," an initial one-electron reduction is formally assumed, followed by protonation to form carboxy (OCOH) species (Scheme 1, left; graphical abstract, b_1 and b_2).

The H_2CO pathway assumes associative reactions. Three coupled proton-electron transfer steps to OCOH progressively form formic acid, dihydroxymethin ($HC(OH)_2$), H_2CO, and water. A subsequent associative route yields CH_3OH, methyl species, and CH_4 (Scheme 1, left). Overall, the H_2CO pathway is thermodynamically feasible.[5]

In the associative pathway, intermediate H_2CO is highly unstable. Consequently, further hydrogenation proceeds readily. As a result of multiple hydrogenations, CH_3OH is thermodynamically more favorable than CH_4, based on the energetics in Equations 2 and 3:

$$CO_2(g) + 2H_2O(g) \rightarrow CH_3OH(g) + \frac{3}{2}O_2(g), \Delta_r H^{\ominus} = 676.49\ \text{kJ mol}^{-1} \quad \text{(Equation 2)}$$

and

$$CO_2(g) + 2H_2O(g) \rightarrow CH_4(g) + 2O_2(g), \Delta_r H^{\ominus} = 802.34\ \text{kJ mol}^{-1}. \quad \text{(Equation 3)}$$

Accordingly, further CH_4 formation from CH_3OH in the H_2CO pathway (Scheme 1, left) must be evaluated using E_{act} values and kinetic experiments, such as those using ^{13}C-methanol under photocatalytic CO_2 reduction conditions or via DFT calculations.

$\ddot{C}$ pathway

In contrast to the H_2CO pathway, the classic $\ddot{C}$ pathway of CO_2 photoreduction also formally assumes an initial one-electron CO_2 reduction, followed by coupled proton-electron transfer to form CO and hydroxy species dissociatively (Scheme 1, right; graphical abstract, c_1 and c_2).[4] However, if coupled proton-electron transfer occurs directly to CO_2, the electrochemical potential is reduced from −1.9 V (Equation 1) to

$$CO_2 + 2H^+ + 2e^- \rightarrow CO + H_2O, E^{\ominus} = -0.53\ \text{V @ pH 7} \quad \text{(Equation 4)}$$

by 1.4 V.[6] Similarly, via the next two steps, CO is reduced to $\ddot{C}$ and hydroxy species (Scheme 1, right). Carbene is progressively hydrogenated to CH_4, while the coupling of methyl species with hydroxy to form CH_3OH is unlikely in the dissociative pathway.

Please cite this article in press as: Sasaki et al., Density functional theory-guided C–C coupling pathways in photocatalytic CO_2 reduction to C_2–C_3 products, Chem Catalysis (2026), https://doi.org/10.1016/j.checat.2026.101846

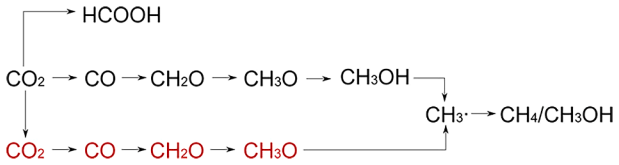

Scheme 2. Mechanism for the photoreduction of CO_2
Black species are located on 5-fold Ti, while red species are located on $V_O^{\cdot\cdot}$ sites. Reprinted with permission from Ji and Luo.[5] Copyright 2016 American Chemical Society.

Hypothesis of surface contribution to the pathways

The classical H_2CO and $\ddot{C}$ pathways described above represent general CO_2 photoreduction or electroreduction routes, focusing primarily on reactant transformation. However, from the perspective of surface science and catalysis, surface site differences are critical. The difference between the surface 5-fold Ti site and the surface O vacancy ($V_O^{\cdot\cdot}$ in Kröger-Vink notation: $V^{\text{number of electrons dispersed as dots}}_{\text{element symbol lost at the site}}$) site at the anatase-phase (a-)TiO_2 (1 0 1) was evaluated for both pathways, using the generalized gradient approximation + Hubbard *U* parameter (4.0 eV) with the Heyd-Scuseria-Ernzerhof functional, including transition-state searches via CI-NEB, in 2016 (supplemental information, Section S1).[5] In that study, the associative route from carboxy to formic acid was rejected owing to high E_{act}, methoxy intermediate was assumed in place of $H_2\dot{C}OH$ species (Scheme 1, left), and an alternative route via CO was proposed as the modified H_2CO pathway (Scheme 2). In particular, the pathway involving $V_O^{\cdot\cdot}$ sites was carefully verified using E_{act} values: 0.73 eV (CO_2 to CO), 0.81 eV (CO to HCO^-), 0.33 eV (HCO^- to H_2CO), 1.26 eV (H_2CO to H_3CO^-), 0.63 eV (H_3CO^- to $\cdot CH_3$), and 0.71 eV (CH_3^- to CH_4)—all of which are lower than the maximum E_{act} value (1.41 eV) for reaction steps occurring over the 5-fold Ti site without $V_O^{\cdot\cdot}$.

In the carbene pathway, CO-to-carbene conversion was ruled out on 5-fold Ti and $V_O^{\cdot\cdot}$ sites owing to its strongly endothermic (endergonic) nature. The carbene pathway was, therefore, excluded in the study by Ji et al.[5] However, surface-site effects were considered: the carbene pathway over the 5-fold Ti site can be regarded as equivalent to the H_2CO pathway over the $V_O^{\cdot\cdot}$ site if CO adsorbed over the $V_O^{\cdot\cdot}$ site suitably positions C species over the 5-fold Ti site.

Via the H_2CO mechanism, CH_3OH was generated via $CO_2 \rightarrow HCO_2H \rightarrow H_2CO \rightarrow CH_3OH$ and subsequently converted to CH_4 (Scheme 1, left).

Via the carbene mechanism, CO is converted to C·, CH_3·, and CH_3OH/CH_4 as final products (Scheme 1, right). In actual reactions, competition exists between the H_2CO and carbene mechanisms, and the final product is determined by the dominant pathway. Another study by Ji et al.[7] suggests that on an ideal surface, the reaction proceeds via $CO_2 \rightarrow H_2CO \rightarrow CH_3OH \rightarrow CH_4$, whereas on $V_O^{\cdot\cdot}$ sites, the pathway follows $CO_2 \rightarrow CO \rightarrow H_2CO$

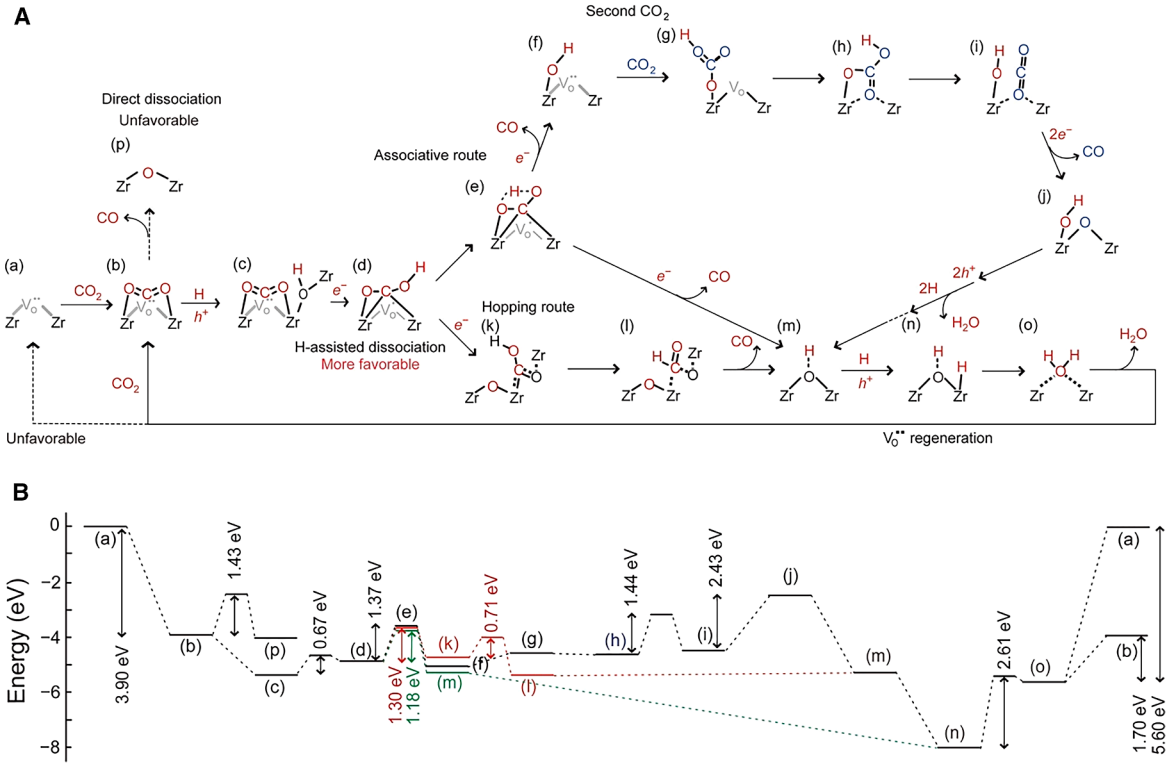

Scheme 3. Reaction pathway from CO_2 to CO using ZrO_2
Proposed reaction pathways (A) and energetics of CO_2 photoreduction facilitated by the $V_O^{\cdot\cdot}$ site on the monoclinic ZrO_2 (1 1 1) surface (B). Reprinted with permission from Hara et al.[9] Copyright 2023 American Chemical Society.

Please cite this article in press as: Sasaki et al., Density functional theory-guided C–C coupling pathways in photocatalytic CO_2 reduction to C_2–C_3 products, Chem Catalysis (2026), https://doi.org/10.1016/j.checat.2026.101846

Table 1. Reported highest E_{act} by CI-NEB method and highest thermodynamic potential-determining steps by $\Delta_r G$-based profile in the CO_2 reduction pathways using photocatalysts

		Barrier/potential determining step in the reduction path					
Entry	Photocatalyst	Step	E_{act} (eV) by CI–NEB	Highest $\Delta_r G$ (eV)	Products	Reference	Diagram
a	TiO_2-$V_O^{\cdot\cdot}$	$CH_2O \rightarrow CH_3O$	1.26	–	CH_4, CH_3OH	Ji et al.[5]	–
b	TiO_2	$CO_2 \rightarrow OCOH$	1.41	–	CO	Ji et al.[7]	Figure 1
c	Cu_2O	$OCOH \rightarrow H_2O(l) + CO$	–	0.77	CH_4, CH_3OH	Chen et al.[8]	Figure 3
c'	Cu_2O-$V_O^{\cdot\cdot}$	$CO \rightarrow CHO$	–	0.73	CH_4, CH_3OH	Chen et al.[8]	Figure 3
d	ZrO_2	$OCOH \rightarrow OH + CO$	1.18	–	CO	Hara et al.[9]	Scheme 3
e	Ni–ZrO_2	$CO_2 \rightarrow OCOH$	1.40	–	CH_4	Hara et al.[9]	Scheme 5
f	Ti–C_4N_3	$CH_3 \rightarrow CH_4$	1.0	–	CH_4	Sun et al.[10]	Scheme 6
f'	Ti–C_4N_3	$C_2H \rightarrow C_2H_2$	3.3	–	C_2H_6	Sun et al.[10]	Scheme 6
g	Pd_{NC}–Pd_{SA}–CeO_2-$V_O^{\cdot\cdot}$	$CO_2 \rightarrow OCOH$	–	0.72	C_2H_6	Duan et al.[11]	Figure 5
h	Cu–halogen–thiophene pol.	HOHC–COH → HC–COH	–	1.12	C_2H_6	Yang et al.[12]	Figure 6
i	Co–ZrO_2	$CO_2 \rightarrow OCOH$	1.30	–	CH_4, C_2H_6	Loumissi et al.[13]	Figure 7
j	Ti–O_xN_y-$V_O^{\cdot\cdot}$	$2CO \rightarrow OC–CO$	–	0.53	C_2H_4	Ni et al.[14]	Figure 8
k	In–$V_S^{\cdot\cdot}$–Bi_2S_3	$CO_2 \rightarrow OCOH$	–	0.94	C_2H_4	Yan et al.[15]	Figure 9
l	Cu–TiO_2	$2CO \rightarrow OC–CO$	–	0.85	C_2H_4	Wang et al.[16]	Figure 10
l'	Cu–Ce_2–TiO_2	$2CO \rightarrow OC–CO$	–	0.81	C_2H_4	Wang et al.[16]	Figure 10
m	Cu–CeO_2-$V_O^{\cdot\cdot}$	$2CO \rightarrow OC–CO$	–	0.61	C_2H_4	Liu et al.[17]	Figure 11
n	MgFe–COF	$CO_2 \rightarrow OCOH$	–	0.41	C_2H_4	Chen et al.[18]	Figure 12
o	$NiMn_2$–MIL	$HO–CH_2CH_2O \rightarrow CH_2CH_2O$	–	1.1	C_2H_4	Wu et al.[19]	Figure 13
o'	$NiMn_2$–MIL	$OC–CH_2O + CO \rightarrow OC–CO–CH_2O$	–	0.47	C_3H_8	Wu et al.[19]	Figure 13
p	$CuGaS_2$–CuO	$CHO \rightarrow CHOH$	–	0.61	C_2H_4	Chakraborty et al.[20]	Figure 14
q	$In_{2.77}S_4$–COF	$CO_2 \rightarrow OCOH$	–	0.73	C_2H_4	Das et al.[21]	Figure 15
r	Bi_2O_3@Bi_2S_3	$CO \rightarrow COH$	–	1.9	C_2H_4	Zhang et al.[22]	Figure 16
s	Cu–In/Ti–BPDC	$CO_2 \rightarrow OCOH$	–	1.37	C_2H_4, C_2H_5OH	Wang et al.[23]	Scheme 7
t	Cu–NH_2–BTC@TiO_2	$OCOH \rightarrow OH + CO$	–	1.93	C_2H_5OH	Xia et al.[24]	Scheme 8
u	TiO_{2-x}–BN	$CHO + CO \rightarrow OC–CHO$	–	0.56	C_2H_5OH	Liu et al.[25]	Figure 17
v	amorp. Pd–$Cd_{0.9}Zn_{0.1}S$	$2CO \rightarrow OC–CO$	–	0.56	C_2H_5OH	Xue et al.[26]	Scheme 9
w	O-doped, N-defec. org. comp.	$OC–COH \rightarrow C–CO$	–	1.44	C_2H_5OH	Tan et al.[27]	Scheme 10
x	Co_{SA}–black P	$OCOH \rightarrow HCO_2H$	0.29	–	HCO_2H	Sun et al.[28]	Figure 18
x'	Co_{SA}–black P	$CHCH_2OH \rightarrow CHCH_2OH$	0.33	–	C_2H_4	Sun et al.[28]	Figure 18

$\rightarrow CH_3 \rightarrow CH_4/CH_3OH$, suggesting that the presence of $V_O^{\cdot\cdot}$ sites alters the dominant reaction pathway.

ADJUSTED, RECENT HYPOTHESES RELATED TO EXPERIMENTS

Pathways to CO

OCOH intermediate

In the CO_2-to-CO reduction pathways, OCOH and its isomer OCHO (formate) have been frequently reported (graphical abstract, a, b_1, and b_2). Over the Cu_2O (1 1 0) surface, OCOH is more favorable than OCHO[8] because CO_2 adsorbs as η_1-C on the surface O atom. Hydrogenation at the C atom—coordinated with three O atoms—requires dissociation of the C–surface O bond to form OCHO, whereas hydrogenation at the terminal O atom is more plausible (Equation 5; Table 2, row h):

$$O_2C - O(\text{surface}) + H(\text{ads}) \rightarrow O(HO)C - O(\text{surface}). \quad \text{(Equation 5)}$$

The formation of OCOH in the CO_2-to-CO reduction[8] pathway was also reported over the monoclinic-phase (m-)ZrO_2 (1 1 1) surface comprising $V_O^{\cdot\cdot}$ sites (Table 2, row m).[9] CO_2 adsorbed most stably at the $V_O^{\cdot\cdot}$ site of original $(\mu\text{-Zr})_2$ coordination with an adsorption energy of −3.9 eV (Scheme 3B), and hydrogenation of CO_2 adsorbed to OCOH proceeded with an E_{act} = 0.67 eV (Scheme 3, c and d). As summarized in Table 1,

Please cite this article in press as: Sasaki et al., Density functional theory-guided C–C coupling pathways in photocatalytic CO_2 reduction to C_2–C_3 products, Chem Catalysis (2026), https://doi.org/10.1016/j.checat.2026.101846

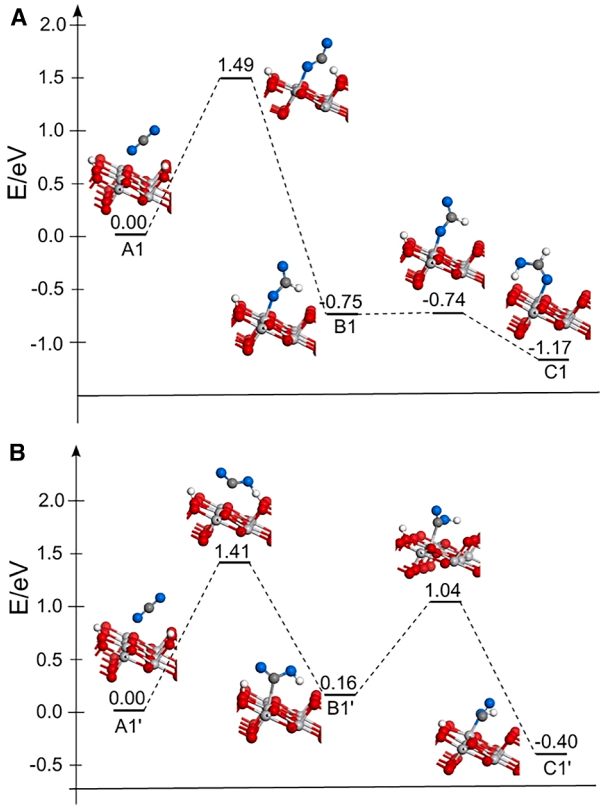

Figure 1. Calculated energy changes in the photoreduction of CO_2 to CO on an anatase TiO_2 (1 0 1) surface

CO_2 to HCO_2H (A) and CO_2 to CO (B). Color key: blue O of O_2; red, O of TiO_2; gray, Ti; and dark gray, C atoms.

Reprinted with permission from Ji and Luo.[7] Copyright 2016 American Chemical Society.

OCOH is the key intermediate in most DFT-calculated reports on CO_2 photoreduction.

Pathways from OCOH to CO

Pathways from OCOH to CO have been reported. Over the a-TiO_2 (1 0 1) surface, following the step from CO_2 to OCOH (E_{act} = 1.41 eV), the energy barrier for OCOH splitting into CO and OH was lower (E_{act} = 0.88 eV), making CO formation favorable (Figure 1B; Table 2, rows c and d).[7]

Over the *m*-ZrO_2 (1 1 1) surface comprising $V_O^{\cdot\cdot}$ sites, a four-membered-ring OCOH intermediate was proposed to split to CO and OH (Scheme 3A, d and e).[9] The E_{act} was suppressed to 1.18 eV by the $V_O^{\cdot\cdot}$ site accommodating the split OH species (Scheme 3B, d, e, and m; Table 1, row d; Table 2, row m).

Pathways to CH_4 and/or CH_3OH

Effects of $V_O^{\cdot\cdot}$ sites on CO intermediate formation

Cu_2O has been reported for photoreduction of CO_2 to CH_3OH.[29] When a $V_O^{\cdot\cdot}$ site is created at the Cu_2O (1 1 0) surface, the terminal O atom of adsorbates tends to be accommodated at the $V_O^{\cdot\cdot}$ site upon adsorption. Accordingly, CO_2 adsorbed at the $V_O^{\cdot\cdot}$ site adopts a structure equivalent to CO adsorbed on a surface O atom (Scheme 4, left; Table 2, row k). Subsequent CO hydrogenation yields CHO and HC–OH intermediates, leading to CH_4 and CH_3OH formation (Scheme 4).[8]

COH and/or CHO intermediates

Over the Cu_2O (1 1 0) surface, COH was formed via OCOH dissociation (OCOH → CO + OH), followed by CO hydrogenation (CO + H → COH; Table 2, row i), with reaction Gibbs energy $\Delta_r G$ = 0.87 eV. An alternative hydrogenation pathway yielded CHO (graphical abstract, e), with a lower and favored $\Delta_r G$ of 0.73 eV.[8]

Over the *m*-ZrO_2 (1 1 1) surface, the photocatalytic CO_2 reduction product was exclusively CO,[9] as illustrated in Scheme 3 and Table 2 (row n). It is worth noting that the final large desorption energy of H_2O can be compensated by the adsorption energy of CO_2 on the same site.[9] To produce CH_4, ZrO_2 was combined with Ni nanoparticles. Notably, COH species were preferred over the ZrO_2 surface and transferred to the neighboring Ni surface, with an E_{act} = 0.32 eV (Schemes 5A and 5B, d' and s; Table 2, row o).[9]

HCO_2H intermediates

Over the a-TiO_2 (1 0 1) surface, the H_2CO pathway was followed. For CO_2 photoreduction to HCO_2H, two electrons were

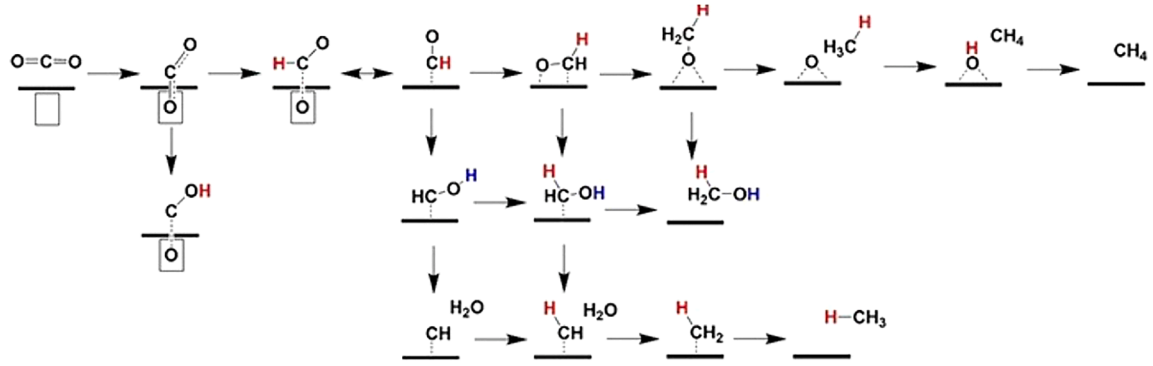

Scheme 4. Dominant reaction pathway and key intermediates for CO_2 reduction on slightly reduced Cu_2O (1 1 0) surface

Reprinted with permission from Chen et al.[8] Copyright 2023 Wiley-VCH.

Please cite this article in press as: Sasaki et al., Density functional theory-guided C–C coupling pathways in photocatalytic CO_2 reduction to C_2–C_3 products, Chem Catalysis (2026), https://doi.org/10.1016/j.checat.2026.101846

Table 2. Reported reaction pathways, the active sites, and E_{act} values using photocatalysts for CO_2 photoreduction

Entry	Pathway	Act site	E_{act} (eV)	Photocatalyst	Activity and selectivity	Products	Section	Reference
a	$CO_2 \rightarrow CH_3O$	$V_O^{\cdot\cdot}$	1.26	a-TiO_2 (1 0 1)	(model surface)	CH_4, CH_3OH	hypothesis of surface contribution to the pathways	Ji et al.[5]
b	$CH_3O \rightarrow CH_4$	Ti	0.71	a-TiO_2 (1 0 1)	(model surface)	CH_4, CH_3OH	hypothesis of surface contribution to the pathways	Ji et al.[5]
c	$CO_2 \rightarrow OCOH$	Ti	1.41	a-TiO_2 (1 0 1)	(model surface)	CH_3OH	pathways from OCOH to CO	Ji et al.[7]
d	$OCOH \rightarrow CO$	Ti	0.88	a-TiO_2 (1 0 1)	(model surface)	CH_3OH	pathways from OCOH to CO	Ji et al.[7]
e	$CO_2 \rightarrow HCO_2H$	Ti	1.49	a-TiO_2 (1 0 1)	(model surface)	CH_3OH	HCO_2H intermediates	Ji et al.[7]
f	$HCO_2H \rightarrow H_2CO$	Ti	1.81	a-TiO_2 (1 0 1)	(model surface)	CH_3OH	HCO_2H intermediates	Ji et al.[7]
g	$H_2CO \rightarrow CH_3OH$	Ti	0.60	a-TiO_2 (1 0 1)	(model surface)	CH_3OH	pathways from H_2CO to CH_3OH	Ji et al.[7]
h	$CO_2 \rightarrow OCOH$	O	–	Cu_2O (1 1 0)	(model surface)	CH_4, CH_3OH	OCOH intermediate	Chen et al.[8]
i	$OCOH \rightarrow COH$	O	–	Cu_2O (1 1 0)	(model surface)	CH_4, CH_3OH	COH and/or CHO intermediates	Chen et al.[8]
j	$CO_2 \rightarrow CH_3OH$	O	–	Cu_2O (1 1 0)	(model surface)	CH_4, CH_3OH	CH_3 intermediates	Chen et al.[8]
k	$CO_2 \rightarrow CO$	$V_O^{\cdot\cdot}$	–	Cu_2O (1 1 0)	(model surface)	CH_4, CH_3OH	effects of $V_O^{\cdot\cdot}$ sites on CO intermediate formation	Chen et al.[8]
l	$CO \rightarrow CH_4$	$V_O^{\cdot\cdot}$	–	Cu_2O (1 1 0)	(model surface)	CH_4, CH_3OH	CH_3 intermediates	Chen et al.[8]
m	$CO_2 \rightarrow OCOH$	$V_O^{\cdot\cdot}$	0.67	*m*-ZrO_2 (1 1 1)	0.80 μmol h^{-1} g_{cat}^{-1}, 100%	CO	OCOH intermediate	Hara et al.[9]
n	$OCOH \rightarrow CO$	$V_O^{\cdot\cdot}$	1.18	*m*-ZrO_2 (1 1 1)	0.80 μmol h^{-1} g_{cat}^{-1}, 100%	CO	pathways from OCOH to CO; COH and/or CHO intermediates	Hara et al.[9]
o	$OCOH \rightarrow CH_4$	Ni	1.40	Ni–m-ZrO_2 (1 1 1)	0.98 mmol h^{-1} g_{cat}^{-1}, 100%	CH_4	COH and/or CHO intermediates; CH_3 intermediates	Hara et al.[9]
p	$CO_2 \rightarrow C_2H_6$	Co	1.30	Co–m-ZrO_2 (1 1 1)	4.1 μmol h^{-1} g_{cat}^{-1}	C_2H_6	CH_3–CH_3 coupling (over Co)	Loumissi et al.[13]
q	$CO_2 \rightarrow C_2H_6$	Ti	3.3	Ti–C_4N_3	(model surface)	C_2H_6	CO_2–CO_2 coupling	Sun et al.[10]
r	$CO_2 \rightarrow C_2H_6$	Pd	–	Pd_{NC}–Pd_{SA}–CeO_2-$V_O^{\cdot\cdot}$	80.4%	C_2H_6	CO–CO coupling	Duan et al.[11]
s	$CO_2 \rightarrow C_2H_6$	Cu	–	Cu–halogen–thiophene pol.	82.3 μmol h^{-1} g_{cat}^{-1}, 77.6%-e^-	C_2H_6	CO–CHO coupling	Yang et al.[12]
t	$CO_2 \rightarrow C_2H_4$	Ti, N	–	TiO_xN_y-$V_O^{\cdot\cdot}$	1.88 μmol h^{-1} g_{cat}^{-1}	C_2H_4	CO–CO coupling	Ni et al.[14]
u	$CO_2 \rightarrow C_2H_4$	Bi, In	–	In–$V_S^{\cdot\cdot}$–Bi_2S_3	11.8 μmol h^{-1} g_{cat}^{-1}, 86%	C_2H_4	CO–CO coupling	Yan et al.[15]
v	$CO_2 \rightarrow C_2H_4$	Cu, Ce	–	Cu–Ce_2–TiO_2	4.51 μmol h^{-1} g_{cat}^{-1}, 47.5%	C_2H_4	CO–CO coupling	Wang et al.[16]
w	$CO_2 \rightarrow C_2H_4$	Ce, Cu	–	Cu–CeO_2-$V_O^{\cdot\cdot}$	31.4 μmol h^{-1} g_{cat}^{-1}, 56.6%	C_2H_4	CO–CO coupling	Liu et al.[17]
x	$CO_2 \rightarrow C_2H_4$	Fe, Mg	–	MgFe–COF	(model surface)	C_2H_4	CO–CHO coupling	Chen et al.[18]
y	$CO_2 \rightarrow C_2H_4$	Ni, Mn	–	$NiMn_2$–MIL	32.2 μmol h^{-1} g_{cat}^{-1}, 81.3%-e^-	C_3H_8	CO–CHO coupling	Wu et al.[19]

(*Continued on next page*)

Table 2. *Continued*

Entry	Pathway	Act site	E_{act} (eV)	Photocatalyst	Activity and selectivity	Products	Section	Reference
ζ	$CO_2 \rightarrow C_2H_4$	Cu^{I}, Cu^{II}	–	$CuGaS_2$–CuO	20.6 μmol h^{-1} g_{cat}^{-1}, 75.1%	C_2H_4	CO–CHOH coupling	Chakraborty et al.[20]
α	$CO_2 \rightarrow C_2H_4$	In, S	–	$In_{2.77}S_4$–COF	67.5 μmol h^{-1} g_{cat}^{-1}, 98.9%-e^-	C_2H_4	CO–COH coupling	Das et al.[21]
β	$CO_2 \rightarrow C_2H_4$	Bi	–	Bi_2O_3@Bi_2S_3	0.22 μmol h^{-1} g_{cat}^{-1}, 39%	C_2H_4	CO–COH coupling	Zhang et al.[22]
γ	$CO_2 \rightarrow C_2H_4$	Cu, In	–	Cu–In/Ti–BPDC	(model surface)	C_2H_4	CHO–CHO coupling	Wang et al.[23]
δ	$CO_2 \rightarrow C_2H_5OH$	Cu	–	Cu–NH_2–BTC@TiO_2	1.29 μmol h^{-1} g_{cat}^{-1}	C_2H_5OH	pathways to C_2H_5OH	Xia et al.[24]
ε	$CO_2 \rightarrow C_2H_5OH$	Ti	–	TiO_{2-x}–BN	51.4 μmol h^{-1} g_{cat}^{-1}	C_2H_5OH	pathways to C_2H_5OH	Liu et al.[25]
ζ	$CO_2 \rightarrow C_2H_5OH$	Pd	–	amorp. Pd–$Cd_{0.9}Zn_{0.1}S$	412 μmol h^{-1} g_{cat}^{-1}, 96.5%	C_2H_5OH	pathways to C_2H_5OH	Xue et al.[26]
η	$CO_2 \rightarrow C_2H_5OH$	N	–	O-doped, N-defect. org. comp.	0.80 mmol h^{-1} g_{cat}^{-1}. 90%	C_2H_5OH	pathways to C_2H_5OH	Tan et al.[27]
θ	$CO_2 \rightarrow HCO_2H$	Co	0.29	Co_{SA}–black P	(model surface)	HCO_2H	DFT approaches to photocatalysis-specific factors	Sun et al.[28]
ι	$CO_2 \rightarrow C_2H_4$	Co	0.33	Co_{SA}–black P	(model surface)	C_2H_4	DFT approaches to photocatalysis-specific factors	Sun et al.[28]

transferred to CO_2 along with proton formation; CO_2 was then reduced to HCO_2 (formate) by combining with the proton. HCO_2 was spontaneously reduced to HCO_2H (formic acid; Figure 1A; Table 2, row e). The two-electron reduction of CO_2 required 1.49 eV; however, subsequent steps to HCO_2H were essentially exergonic.[7]

Notably, Ji et al.[7] examined the two-electron reduction pathway by accommodating intermediate species with two H^+ species in proximity, whereas the one-electron reduction pathway accommodated one H^+ in proximity and one H^+ apart (Figure 2). The subsequent reduction of HCO_2H to H_2CO involved two electrons coupled with a proton attack on the C atom, yielding H_2CO and OH^- (Figure 2, black lines; Table 2, row f). However, this step required an E_{act} = 1.81 eV (Figure 2)—greater than the E_{act} of 1.49 eV required via the CO_2-to-HCO_2H pathway (Figure 1A) and the E_{act} of 1.26–1.41 eV required via CO-to-CH_3O pathway (Scheme 2)—suggesting that the pathways in Scheme 2 are favorable and that the H_2CO pathway via HCO_2H is implausible. The reduction steps of H_2CO are discussed in section "pathways from H_2CO to CH_3OH" (Table 2, row g).

CH_3 intermediates

Over the Cu_2O (1 1 0) surface, most C_1 intermediates are bound to the surface O atom, regarded as the reaction site. Unstable adsorbed CO_2 was transformed to OCOH (Figure 3, top left). CO formed with Δ_rG = 0.77 eV (Table 1, row c), and adsorbed CO preferentially formed CHO rather than COH (Table 1, row c'); graphical abstract, b_1). CHO was converted to CHOH (Δ_rG = 0.60 eV) or H_2CO (Δ_rG = 0.62 eV), and subsequent hydrogenation yielded CH_2OH and then CH_3OH (Table 2, row j).[8] CH_4 formation via CH_2 was unlikely because the Δ_rG value from CH_2OH to CH_2 was higher at 0.87 eV (Figure 3, top).

In contrast, when $V_O^{\cdot\cdot}$ sites are present (section "effects of $V_O^{\cdot\cdot}$ sites on CO intermediate formation"; Table 2, row k), CO_2 adsorbed on the $V_O^{\cdot\cdot}$ site is equivalent to CO on the complete surface (Figure 3, bottom). The Δ_rG value from CO to CHO was 0.73 eV (Figure 3, bottom left), and the transformation of the species was exergonic to CH_3O and CH_4 (Table 2, row l), suggesting a favorable reaction pathway compared with that in the absence of $V_O^{\cdot\cdot}$ sites (Figure 3, top).

Over Ni nanoparticle combined with the *m*-ZrO_2 (1 1 1) surface, COH species transferred from the ZrO_2 surface to Ni nanoparticle were progressively hydrogenated, with a maximum E_{act} of 1.40 eV (Table 1, row e) for the step from methine hydroxy (CHOH) to methine and H_2O (Schemes 5A and 5B, t and u); graphical abstract, b_2).[9]

Pathways from H_2CO to CH_3OH

Over the a-TiO_2 (1 0 1) surface, one-electron and two-electron processes were compared starting from the H_2CO formed in section "HCO_2H intermediates" (Table 2, rows f and g). The one-electron reduction (H^+ and $2e^-$ addition) proceeded with an E_{act} = 1.28 eV to CH_3O^- (Figure 4, purple lines), while the two-electron reduction ($2e^-$ addition) proceeded with a lower E_{act} of 0.60 eV (Figure 4, black lines).[7]

Furthermore, the two-electron reduction was strongly exergonic, producing CH_3O^- irreversibly. The species was readily reduced to CH_3OH with an E_{act} = 0.41 eV.

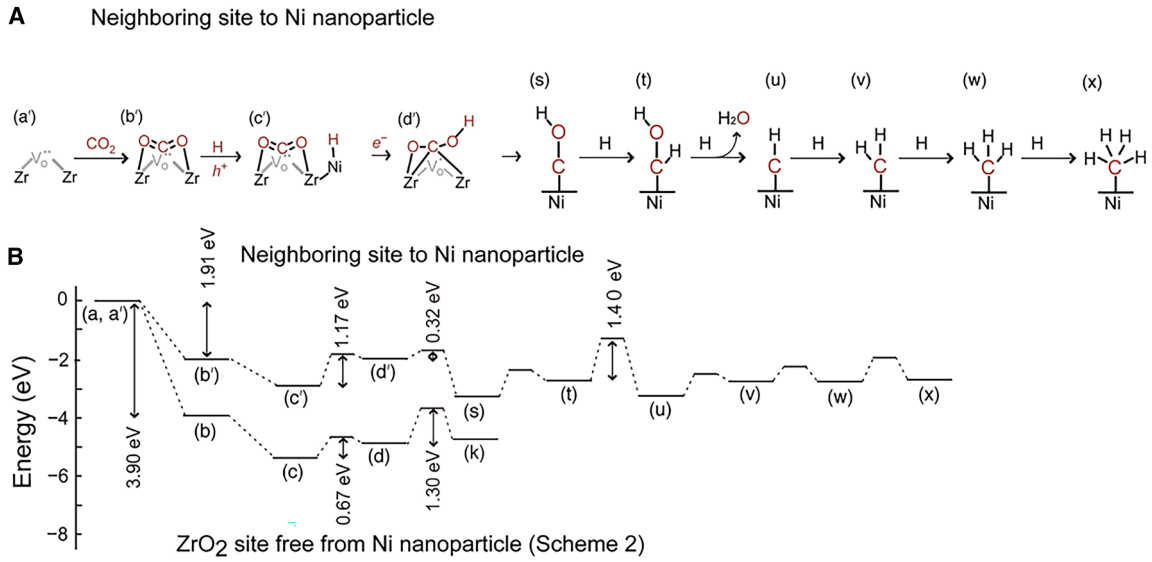

Scheme 5. Reaction pathway from CO_2 to CH_4 using Ni-ZrO_2

Proposed reaction pathways (A) and energetics of CO_2 photoreduction facilitated by the $V_O^{\cdot\cdot}$ site on the ZrO_2 (1 1 1) surface neighboring a Ni nanoparticle (B). Reprinted with permission from Hara et al.[9] Copyright 2023 American Chemical Society.

Pathways to C_2H_6

CO_2–CO_2 coupling

Sustainable CO_2 conversion has been a major topic since 2016, with a growing discussion of the economic feasibility of C-neutral cycles and the effective market prices of CO_2 photoreduction in a sustainable society.[13,30] Thus, C–C coupling has become a critical topic for forming $C_{x \geq 2}$ hydrocarbons, alcohols, and organic acids.

The CO_2 photoreduction pathway using Ti supported on C_4N_3 was theoretically investigated (Table 1, rows f and f'; Table 2, row q).[10] Photocatalytic CH_3OH and CH_4 formations were suggested through OCOH dissociation (Scheme 6, top). Direct coupling of CO_2–CO_2 was also proposed, with an E_{act} of 0.19 eV (Scheme 6, m and f); graphical abstract, g), followed by C_2H_6 formation via oxalic acid (Scheme 6, bottom).

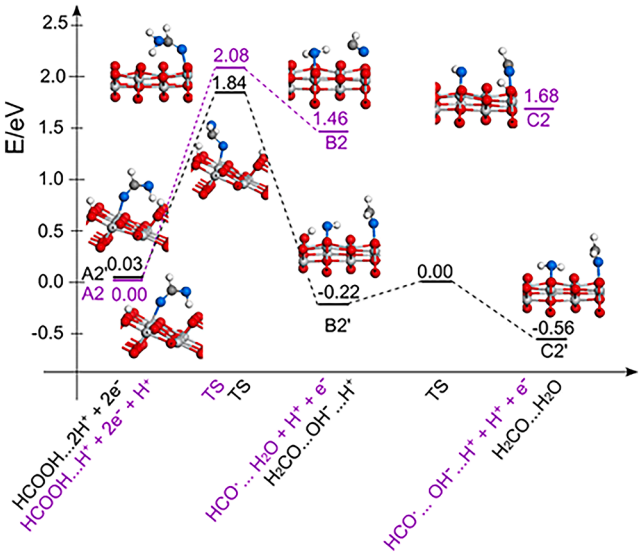

Figure 2. Proposed potential energy surface for the photoreduction of HCO_2H

One electron was transferred in the purple pathway, and two electrons were transferred in the black pathway. Reprinted with permission from Ji and Luo.[7] Copyright 2016 American Chemical Society.

CO–CO coupling

Selective photocatalytic C_2H_6 formation (80.4% on an electron basis) was reported using Pd single atoms and Pd nanoclusters supported on CeO_2 associated with $V_O^{\cdot\cdot}$ sites. $\Delta_r G$ changes were calculated along the reaction coordinate starting from CO_2 on the Pd_4 nanocluster (Figure 5; Table 2, row r); graphical abstract, h). The most exergonic step was the hydrogenation of CO_2 to OCOH on the Pd_4 nanocluster.[11]

The selectivity toward C_2H_6 over CH_4 was attributed to a lower energy barrier for CO–CO coupling leading to C_2H_6 than for CO hydrogenation to formyl species leading to CH_4 (Figure 5, right; graphical abstract, h and f). However, OCOH dissociation to COH (graphical abstract, d) was not reported by Duan et al.[11] The effects of Pd single atoms and $V_O^{\cdot\cdot}$ sites have been suggested to control the Pd nanocluster energy level, governing photocatalytic selectivity.[11]

CO–CHO coupling

Photocatalytic C_2H_6 formation via CO–CHO coupling was reported based on Fourier transform infrared and $\Delta_r G$ changes along the reaction pathway (Table 1, row h; Table 2, row s); graphical abstract, j).[12] Basically, progressive hydrogenation steps were exergonic, whereas dehydroxylation of HO–CH–COH and CH_3–COH and hydrogenation of CH_3–C were endergonic

Please cite this article in press as: Sasaki et al., Density functional theory-guided C–C coupling pathways in photocatalytic CO_2 reduction to C_2–C_3 products, Chem Catalysis (2026), https://doi.org/10.1016/j.checat.2026.101846

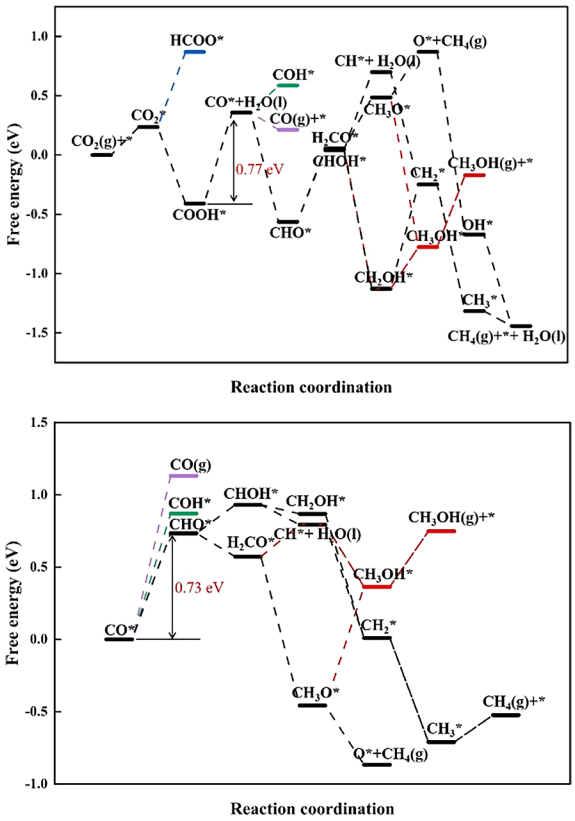

Figure 3. Proposed potential energy surface for the photoreduction of CO_2 on the ideal Cu_2O (1 1 0) surface (top) and the partially reduced Cu_2O (1 1 0) surface (bottom)

Reprinted with permission from Chen et al.[8] Copyright 2023 Wiley-VCH.

(Figure 6). Given the critical dependence of selectivity on CH_4, CO, and C_2H_6, careful tuning is required to achieve C_2H_6 selectivity.

CH_3–CH_3 coupling (over Co)

When an *m*-ZrO_2 (1 1 1) surface was combined with metallic Co nanoparticles, CH_2–CH_2 coupling to C_2H_4 (E_{act} = 0.70 eV) and CH_3–H coupling to CH_4 (E_{act} = 0.93 eV) were demonstrated by CI-NEB (Figure 7), suggesting preferential C_2 formation (graphical abstract, m) over CH_4 starting from CO_2.[13]

Pathways to C_2H_4 and/or C_3H_8

The C–C coupling intermediate step starting from CO_2 is critical for the formation of C_2 and higher-C hydrocarbons compared with CO and/or CH_4 formation. However, the reported species at the C–C coupling step are inconsistent across the literature. The pathways comprising C–C coupling to C_2H_4 and/or C_3H_8 are discussed below.

Experimentally, $C_{2–3}$ paraffin and olefins are often generated simultaneously, and the C–C coupling step is frequently rate determining for their formation (Table 1). Accordingly, later stages of the CO_2 reduction pathway are critical for selectivity toward paraffin, olefins, alcohols, and organic acids.

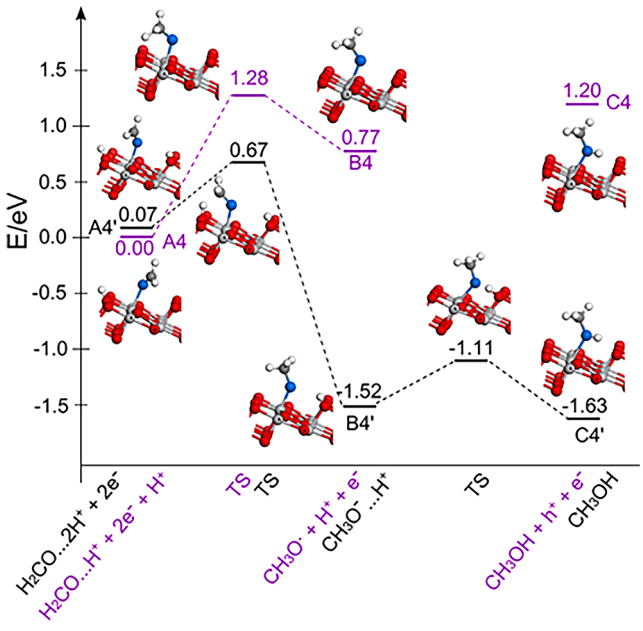

Figure 4. Proposed potential energy surface for the photoreduction of H_2CO

One electron is transferred in the purple pathway, and two electrons are transferred in the black pathway. Reprinted with permission from Ji and Luo.[7] Copyright 2016 American Chemical Society.

CO–CO coupling

Two CO species coupled to OC–CO species with $\Delta_r G$ = 0.53 eV at the $V_O^{\cdot\cdot}$ site on the TiO_xN_y surface (Table 1, row j; Table 2, row t).[14] The OC–CO was spontaneously transformed to OC–CH_2 and then to C_2H_4 based on $\Delta_r G$ changes (Figure 8A; graphical abstract, h). However, identifying the key step in the favorable pathway over TiO_xN_y $V_O^{\cdot\cdot}$ sites requires careful consideration of not only $\Delta_r G$ but also the transition states between CO_2 and OCOH and between two CO molecules and OC–CO (Figure 8A).

CO–CO coupling also occurred over In and Bi atoms at the In–S vacancy ($V_S^{\cdot\cdot}$ in Kröger-Vink notation)–Bi combination site of the Bi_2S_3/In_2S_3 composite (Table 1, row k; Table 2, row u).[15] The coupled CO–CO was nearly spontaneously transformed to OCH–CH_2 species based on $\Delta_r G$ changes (Figure 9A). With $\Delta_r G$ = 0.87 eV, OCH–CH_2 species was hydrogenated to HOCH–CH_2, leading to C_2H_4.[15]

Furthermore, the active site of Cu–Ce–TiO_2 was constructed by substituting Ti sites in a-TiO_2 (1 0 1) with Cu and/or Ce.[16] CO_2 adsorption on the Cu site was facilitated by the neighboring Ce site (Figure 10A, blue lines; Table 2, row v). Hydrogenation of adsorbed CO_2 by H atoms (for example, derived from H_2O) to form carboxy species was exergonic.

H transfer from neighboring adsorbed H_2O to CO_2 to form carboxy was also exergonic. However, caution is required when the calculations such as those in Figure 10 exclude transition states from the reaction coordinate. Careful interpretation of the reaction pathway is, therefore, necessary because a more exergonic pathway (for example, Cu–Ce–TiO_2 in

Please cite this article in press as: Sasaki et al., Density functional theory-guided C–C coupling pathways in photocatalytic CO_2 reduction to C_2–C_3 products, Chem Catalysis (2026), https://doi.org/10.1016/j.checat.2026.101846

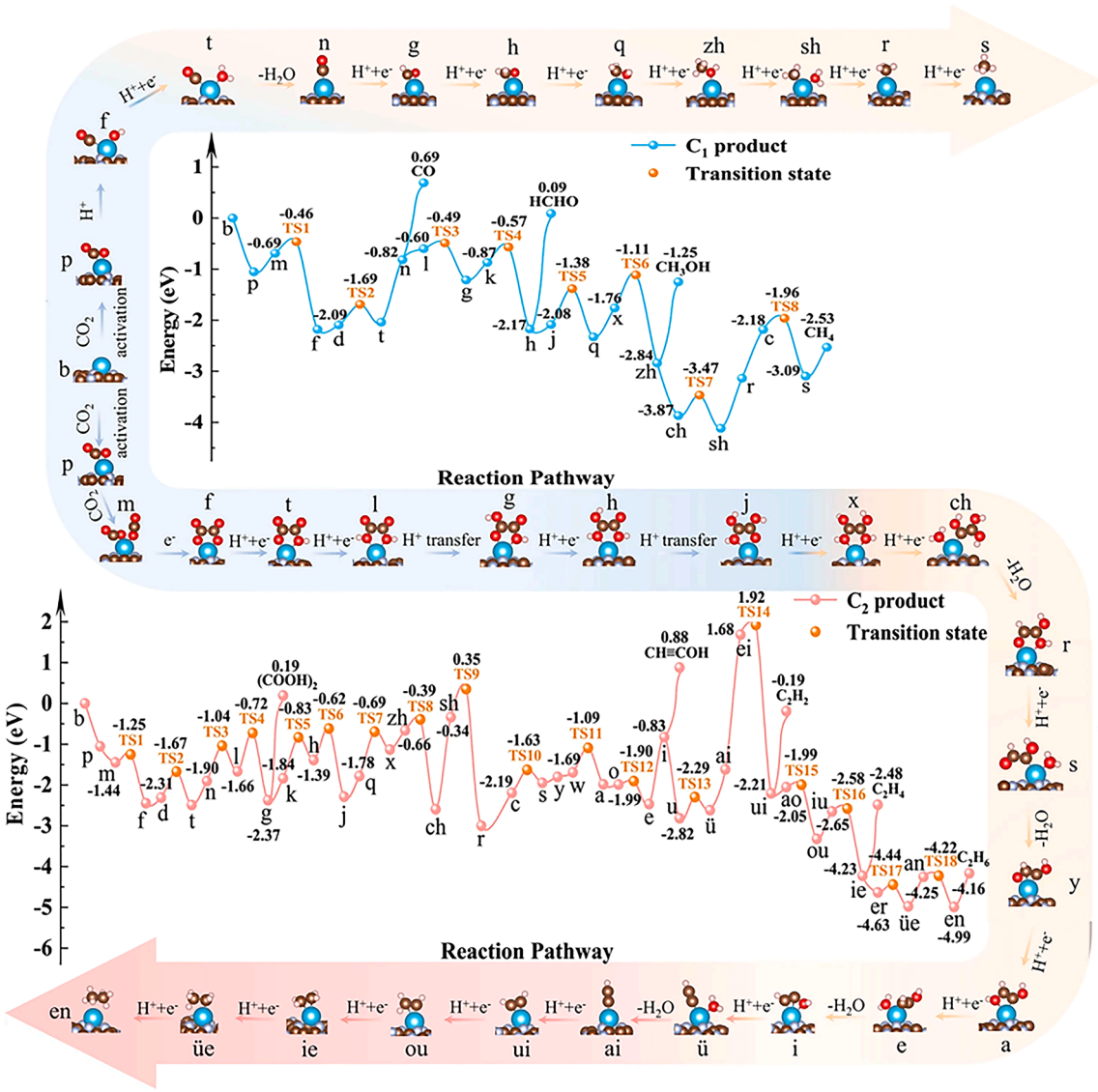

Scheme 6. Energy barrier and reaction intermediates during CO_2 photoreduction to C_1 and C_2 products

b, photocatalyst. Color key: brown, C; silver, N; light blue, Ti; red, O; and white, H. Reprinted from Zhuang and co-workers,[10] licensed under CC BY 4.0.

Figure 9) is not necessarily favorable if the E_{act} value of an exergonic step is high. The $\Delta_r G$ for CO–CO coupling was 0.81 eV, while C_2H_4 desorption was strongly endergonic with $\Delta_r G$ = 3.90 eV (Figures 10A and 10B). As such a large desorption energy is not compatible with experimental C_2H_4 release from the catalyst, the quite exergonic pathway using Cu–Ce–TiO_2 seems to follow too stabilized inert intermediate C_2H_4 species, different from the true pathway leading to gaseous C_2H_4.

The energy change at the CO coupling step at the Cu cluster–CeO_2 surface boundary (1.23 eV) was effectively suppressed to 0.61 eV by introducing a $V_O^{\cdot\cdot}$ site at the boundary and at the CeO_2 surface (Figures 11B and 11C; Table 1, row m; Table 2, row w).[17] Over Cu–CeO_2–$V_O^{\cdot\cdot}$, the subsequent hydrogenation steps from OC–CO to OC–COH and from OC–C to OC–CH were endergonic, while the remaining steps to C_2H_4 were exergonic (Figure 11B).

CO–CHO coupling

Heteronuclear dual metal sites over covalent organic frameworks (COFs) were evaluated by DFT for CO_2 reduction.[18] Seven Cu-based pairs (Cu with Mg, Ca, Mn, Fe, Co, Ni, and Zn) and six Mg-based pairs (Mg with Ca, Mn, Fe, Co, Ni, and Zn) were examined. The Mg–Fe and Mg–Zn pairs—particularly Mg–Fe (Table 2, row x)—were advantageous for CO–CHO coupling (graphical abstract, j) based on negative $\Delta_r G$ for O=(η-C)–CH(η-O) formation relative to CH_2O formation by hydrogenation of CHO species (Figures 12B and 12C), with the subsequent step calculated to selectively yield C_2H_4. Comparatively, (η-O) = C–CH(η-O) formation was unfavorable (Figure 12C).

Please cite this article in press as: Sasaki et al., Density functional theory-guided C–C coupling pathways in photocatalytic CO_2 reduction to C_2–C_3 products, Chem Catalysis (2026), https://doi.org/10.1016/j.checat.2026.101846

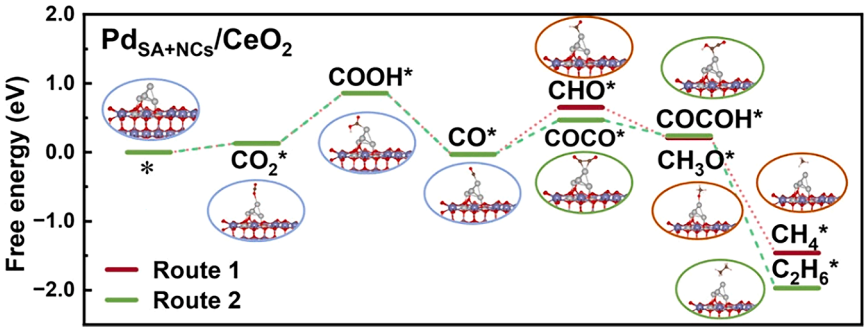

Figure 5. Free energy diagram of CO_2 conversion on photocatalysts and the structure of reaction intermediates of $Pd_{Nanocluster}$–$Pd_{Single\ atom}$–CeO_2

Reprinted with permission from Duan et al.[11] Copyright 2025 American Chemical Society.

Similarly, CO–CHO coupling was calculated to be exergonic over $NiMn_2$–MIL (a metal-organic framework) photocatalyst.[19] Coupling of O=C–CH_2–O with CO to O=C–C(=O)–CH_2–O was the highest Δ_rG (0.47 eV) toward C_3H_8, whereas dehydroxylation of HO–CH_2–CH_2O to CH_2–CH_2O was the relatively high Δ_rG (1.1 eV) toward C_2H_4 (Figure 13; Table 1, rows o and o'), consistent with selective C_3H_8 formation.

CO–CHOH coupling

Direct CO coupling on adjacent Cu^I and Cu^{II} was strongly endergonic (Δ_rG = 1.9 eV; Figure 14A). CO–CHOH coupling to OC–CHOH (graphical abstract, k) was comparatively favorable (Δ_rG = 0.27 eV); the resulting one-electron-reduced HC–CO species was energetically favorable, leading to C_2H_4 mostly exergonic over the Cu^I–Cu^{II} coupled site (Table 1, row p; Table 2, row z).[20]

CO–COH coupling

The reaction pathway for selective C_2H_4 photogeneration from CO_2 dissolved in H_2O using an $In_{2.77}S_4$ photocatalyst combined with a porous organic polymer (POP) was investigated for two models in which the upper surface of $In_{2.77}S_4$ interacted with POP, designated HU1 and HU2 (Figure 15).[21]

Over HU2, adsorbed CO_2 was reduced to unstable carboxy (Δ_rG = 0.73 eV; Table 1, row q), followed by the formation of CO and COH. COH combined with CO over HU1 to form OC–COH (graphical abstract, i). This intermediate was transformed to HOC = COH and C≡COH over HU2, followed by the transformation to HC = COH at the HU1-HU2 boundary (Figure 15A, cycle B). It was reduced to C≡CH over HU1 and progressively hydrogenated to C_2H_4 at the HU1-HU2 boundary (Figure 15A, cycle C).[21]

Similar to CO–CHO coupling over heteronuclear dual metal sites (section "CO–CHO coupling"; graphical abstract, j),[18,19] CO–COH coupling (graphical abstract, i) was calculated to be exergonic on charge-unbalanced Bi_2O_3-Bi_2S_3 heterojunctions, unlike the endergonic behavior on Bi_2O_3 nanosheet and Bi_2S_3 nanorod (Figure 16H).[22] However, the more endergonic hydrogenation step from CO to COH at the Bi_2O_3 and Bi_2S_3 interface was not addressed (Table 1, row r; Table 2, row β).

CHO–CHO coupling

Active sites of Cu–M/Ti–BPDC (M = Sc, Mn, Fe, Cu, Nb, Ru, Rh, Pd, Pt, Os, Ir, In, Sn, and Bi; BPDC = 2,2′-bipyridine-5,5′-dicarboxylic acid) for CO_2 photoreduction were evaluated computationally. Cu–In/Ti–BPDC was identified as the best photocatalyst for CO_2-to-C_2H_4 conversion (Table 2, row γ). The critical C–C coupling step was attributed to CHO on the Cu^+ site and CHO on In^{3+} site rather than CO + CO or CO + CHO (Scheme 7; graphical abstract, l).[23]

Pathways to C_2H_5OH

An amino-functionalized metal-organic framework, NH_2–Cu–benzenetricarboxylic acid (BTC), was grown layer by layer onto TiO_2 nanofibers.[24] The largest energy change (Δ_rG = 1.93 eV) corresponded to OCOH dissociation into CO + OH (Table 1, row t), whereas CO–CO coupling was assumed in the following pathway (Scheme 8). Subsequent associative steps produced C_2H_5OH (graphical abstract, h).

Partially reduced TiO_{2-x} dispersed on boron nitride (BN) photoreduced CO_2 to C_2H_5OH at 51 μmol h^{-1} $g_{cat}{}^{-1}$ (Table 2, row ε).[25] CO–CO coupling with H to OC–CHO on the TiO_{2-x}

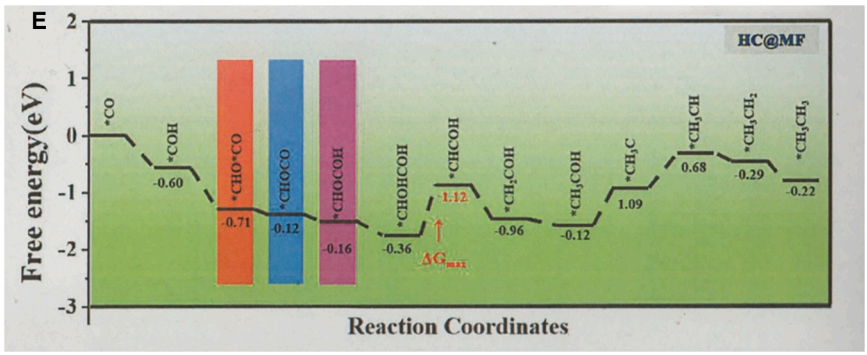

Figure 6. Free energy diagram of CO_2 photoreduction to C_2H_6 on a Cu–halogen–thiophene polymer

Reprinted from Yang et al.[12] Copyright 2026 Elsevier.

Please cite this article in press as: Sasaki et al., Density functional theory-guided C–C coupling pathways in photocatalytic CO_2 reduction to C_2–C_3 products, Chem Catalysis (2026), https://doi.org/10.1016/j.checat.2026.101846

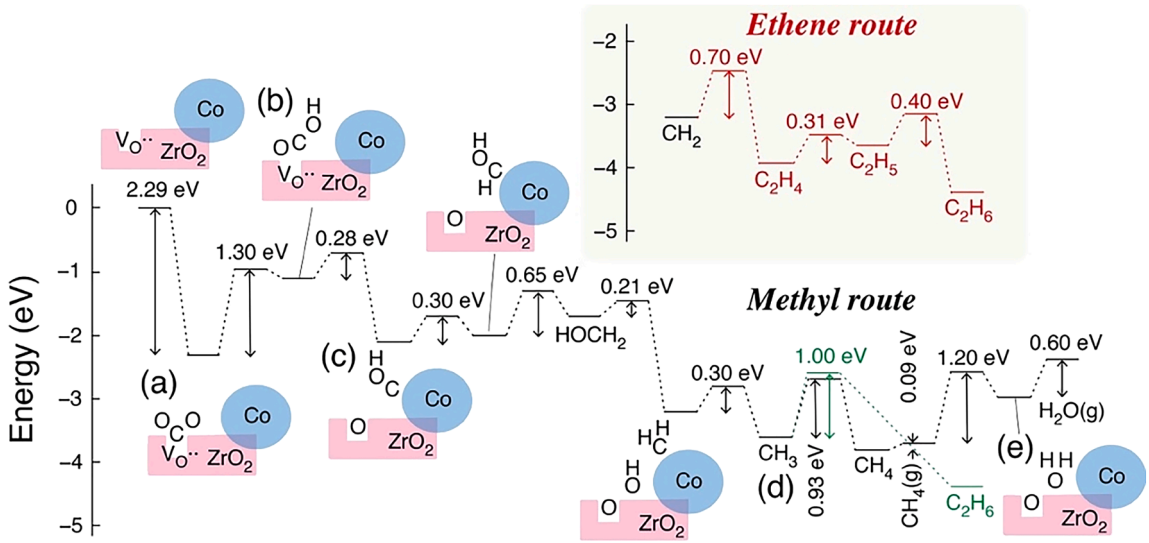

Figure 7. Energy diagram for the *m*-ZrO_2 (1 1 1) surface combined with a Co_{19} cluster exposing an hcp (0 1 0) surface, calculated under CO_2 and H_2

The ethene route is shown in the upper-right inset alongside the methyl route. Reprinted from Loumissi et al.,[13] licensed under CC BY 4.0.

surface was plausible, with $\Delta_r G$ = 0.40 eV (Figure 17A). C_2H_5OH was favored over C_2H_4 in a hydrophilic reaction environment.

As an inorganic photocatalyst, amorphous Pd supported on $Cd_{0.9}Zn_{0.1}S$ nanorods selectively formed C_2H_5OH from CO_2.[26] $\Delta_r G$ value for the CO–CO coupling was markedly suppressed from 2.24 to 0.56 eV when the crystalline Pd was turned into amorphous Pd (Scheme 9; Table 1, row v). Subsequent steps proceeded dissociatively to C=C=O

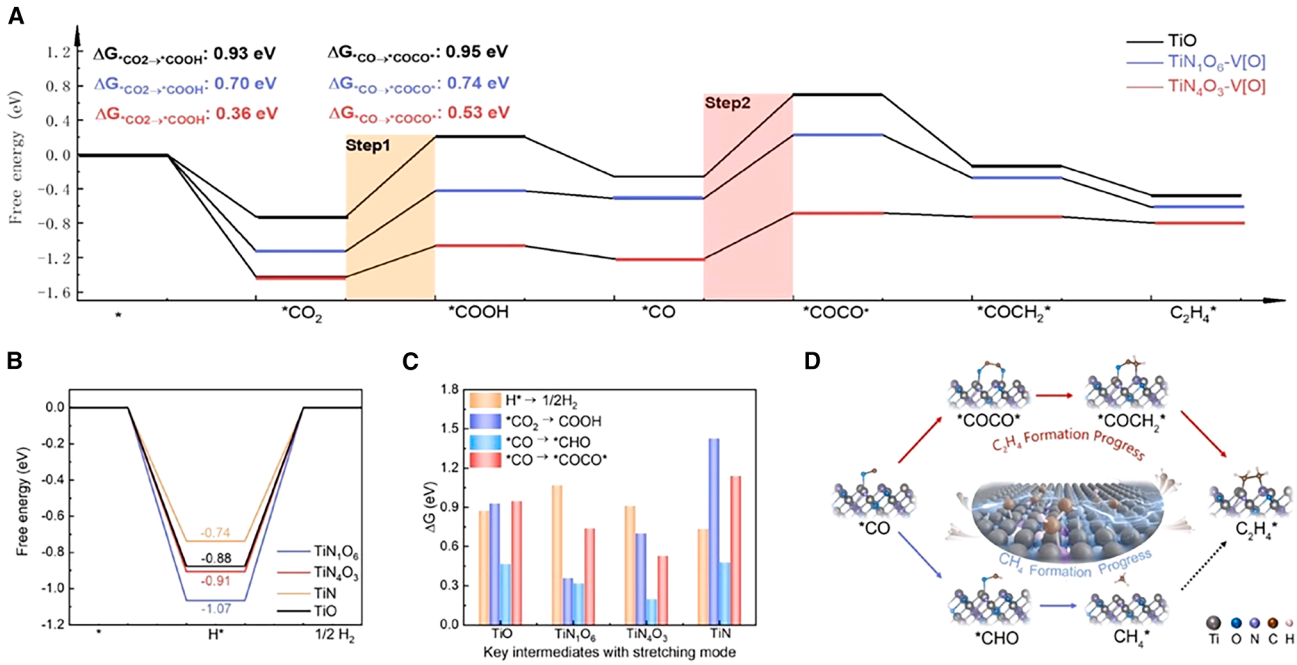

Figure 8. Gibbs free energy profile derived from DFT calculations for TiO_xN_y with different N/O ratios

(A) CO_2 photoreduction to C_2H_4.
(B) H adsorption free energy describing H_2 evolution reaction activity.
(C) Comparison of the free energies of key intermediates in different models.
(D) Representation of C_1 and C_2 pathways in TiO_xN_y–$V_O^{\cdot\cdot}$-catalyzed CO_2 reduction.
Reprinted with permission from Ni et al.[14] Copyright 2023 Wiley-VCH.

Please cite this article in press as: Sasaki et al., Density functional theory-guided C–C coupling pathways in photocatalytic CO_2 reduction to C_2–C_3 products, Chem Catalysis (2026), https://doi.org/10.1016/j.checat.2026.101846

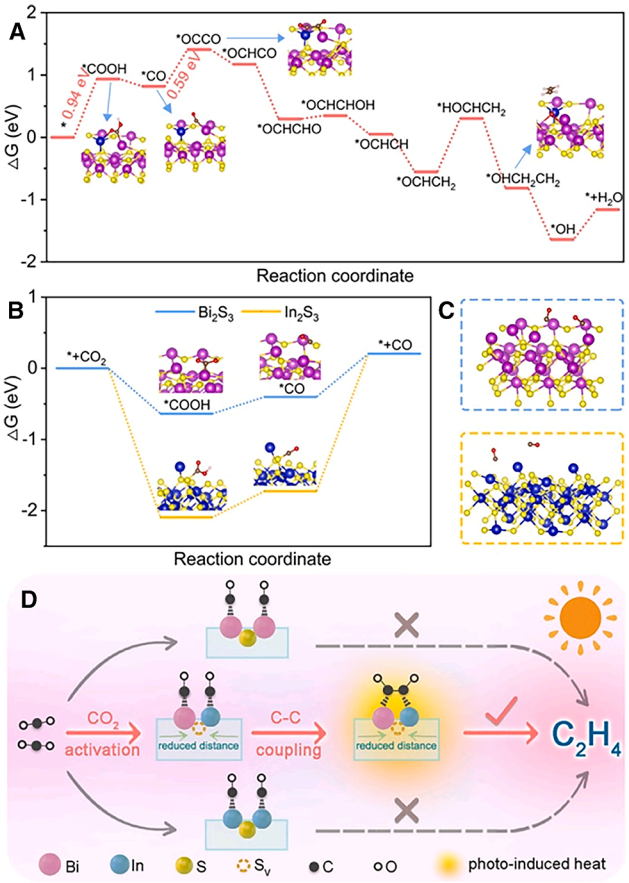

Figure 9. DFT calculations and schematic diagram of catalytic CO_2 reduction to C_2H_4

(A and B) Gibbs free energy diagrams for (A) CO_2 reduction to C_2H_4 on the In–$V_S^{\cdot\cdot}$–Bi_2S_3 surface and (B) CO_2 reduction to CO on pristine Bi_2S_3 and In_2S_3 surfaces.

(C) Configurations of two CO adsorbed on (A) Bi_2S_3 and (B) In_2S_3 surfaces.

(D) Proposed catalytic reaction mechanism for CO_2 reduction on Bi_2S_3@In_2S_3, Bi_2S_3, and In_2S_3.

Reprinted with permission from Yan et al.[15] Copyright 2023 American Chemical Society.

intermediate, after which the later stages proceeded associatively to C_2H_5OH.

Finally, for photocatalytic C_2H_5OH synthesis, an N-defective organic photocatalyst prepared from dicyandiamide and formic acid was tested for CO_2 photoreduction.[27] Selective C_2H_5OH formation and exergonic CO–CO coupling were proposed. However, caution is required, as this process is not necessarily spontaneous; the transition state for OC–CO formation must be evaluated. The greatest Δ_rG value (1.44 eV) was dehydroxylation from OC–COH (or OC–CHO) to OC–C (Scheme 10; Table 1, row w).[27]

Correlations between the pathway based on DFT and experiments

In the whole picture of CO_2 photoreduction pathways (graphical abstract), it was almost common that adsorbed CO_2 was transformed to OCOH species using DFT calculations. Especially, the initial one-electron reduction step was often rate determining and/or thermodynamic potential determining (Table 1, rows b, e, g, i, k, n, q, and s). As shown in Figures 1 and 7 and Scheme 5, OCOH can be regarded as an intermediate unstable species based on E_{act} (1.30–1.41 eV), and the prediction of the reaction pathway from CO_2 to OCOH based on Δ_rG (0.41–1.37 eV) seems acceptable.

Two plausible species via the splitting of OCOH are depicted, CO and COH (graphical abstract, d and e). The path was determined by the types of active sites, e.g., Ti, O, and $V_O^{\cdot\cdot}$ (Table 2, rows d, i, and n). Because the following hydrogenation steps were often exergonic, careful check of E_{act} is required for the steps to separate the formation of CO, CH_4, and CH_3OH. Based on E_{act}, the relatively high selectivity reported in Table 2 (rows n and o) can be correlated with the DFT calculation results.

C–C couplings widely extend the products of CO_2 photoreduction for the applications in sustainable society: CO_2–CO_2, CO–CO, CO–COH, CO–CHO, CO–HCOH, CHO–CHO, and CH_2–CH_2 (graphical abstract, g–m). In fact, the steps were calculated to be thermodynamic potential determining, with the Δ_rG values of 0.53–1.44 eV (Table 2, rows j, l, l', m, u, v, and w). Beyond the qualitative prediction of $C_{x\geq2}$ product, a careful evaluation of E_{act} is again required for the coupling step because the step determines the following pathways to C_2H_4, C_2H_6, C_3H_8, and C_2H_5OH. The other critical point for the selectivity of products is mostly exergonic progressive hydrogenation steps later than the C–C coupling step. These steps also need a careful evaluation of E_{act}. Based on E_{act}, experimentally optimized high selectivity (Table 2, rows r–η) can be correlated with the DFT calculation results.

It is also very interesting to note that C_2H_4 was frequently formed on two different element atoms and/or two atoms at different electronic states—Ti–N, Bi–In, Cu–Ce, Ce–Cu, Fe–Mg, Ni–Mn, Cu^{I}–Cu^{II}, In–S, Bi(O)–Bi(S), and Cu–In—and the selectivity is quite high owing to the electronic tuning of the heteroatomic sites (Table 2, rows t–γ). We limit the scope of this review to theoretical calculations for the CO_2 reduction pathway, and recent examples of the experimental studies on the tuning of two different element atoms and/or two atoms at different electronic states for photocatalysis are noted in Table S1.

DFT approaches to photocatalysis-specific factors

Recently, in addition to the analyses of reaction pathways based on the stability of intermediate species, Δ_rG and/or E_{act}, theoretical analyses are in progress taking the behavior of light-excited carrier and the excited states into account. Previous analyses of reaction pathways could effectively evaluate the thermodynamics and kinetics of CO_2 reduction. However, they are mostly based on calculations for the ground state, and it is not easy to analyze the phenomena characteristic of photocatalysis, e.g., creation and separation of electron-hole pairs under the irradiation of UV-visible and/or infrared light and the transfer of the created charge carrier. These are the key characteristics expected to be solved by DFT calculations under such situations.[31]

Please cite this article in press as: Sasaki et al., Density functional theory-guided C–C coupling pathways in photocatalytic CO_2 reduction to C_2–C_3 products, Chem Catalysis (2026), https://doi.org/10.1016/j.checat.2026.101846

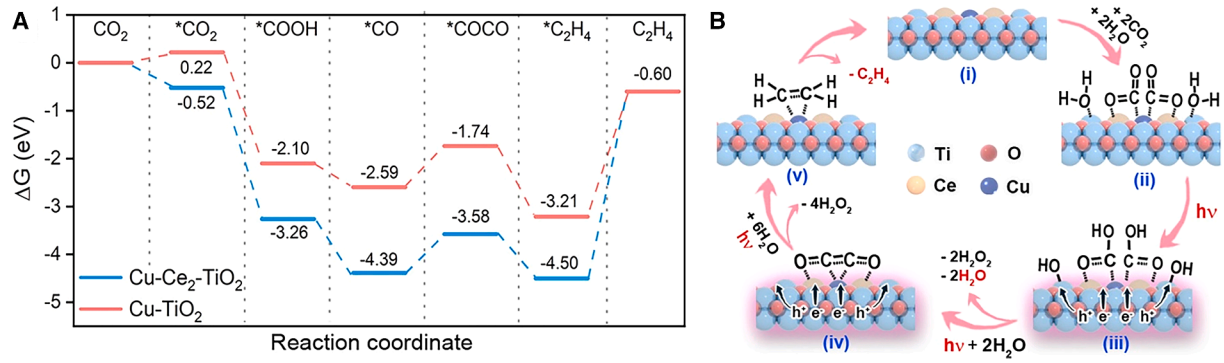

Figure 10. DFT results for the pathway from CO_2 to C_2H_4 over Cu[–Ce_2–]TiO_2

(A) Calculated free energy diagrams for CO_2 reduction over Cu–TiO_2 and Cu–Ce_2–TiO_2 slabs.

(B) Proposed mechanism for photocatalytic CO_2 conversion to C_2H_4.

Reprinted with permission from Wang et al.[16] Copyright 2022 American Chemical Society.

To solve the problem basically depending on the ground-state calculations, band structure and the analysis for the band-edge positions, e.g., valence band maximum and conduction band minimum, and the evaluation of charge transfer based on Bader charge and differential charge density have been conducted for photocatalysts. Furthermore, carrier and molecular dynamics at the excited states by the analyses based on nonadiabatic molecular dynamics (NAMD) and *ab initio* molecular dynamics (AIMD) have been employed to clarify the details of reaction pathways of photocatalysis.

For the single-atom Co photocatalyst supported on black phosphorus (BP), the band structure, band-edge position, density of states, and Bader charge as well as the analysis of carrier life by NAMD, single-atom Co–BP was demonstrated to possess sufficient absorbance of visible light and light-irradiated carrier of enough long life for photocatalysis.[28] That is, based on the analyses of differential charge density and Bader charge upon CO_2 adsorption, CO_2 was activated as a result of the electron transfer from Co to CO_2.

Then, the reaction pathway was evaluated via the CI-NEB method to C_1 products over single-atom Co–BP. The step from CO_2 to OCOH (section "OCOH intermediate") was favored (E_{act} = 0.05 eV) rather than to HCO_2 ("HCO_2H

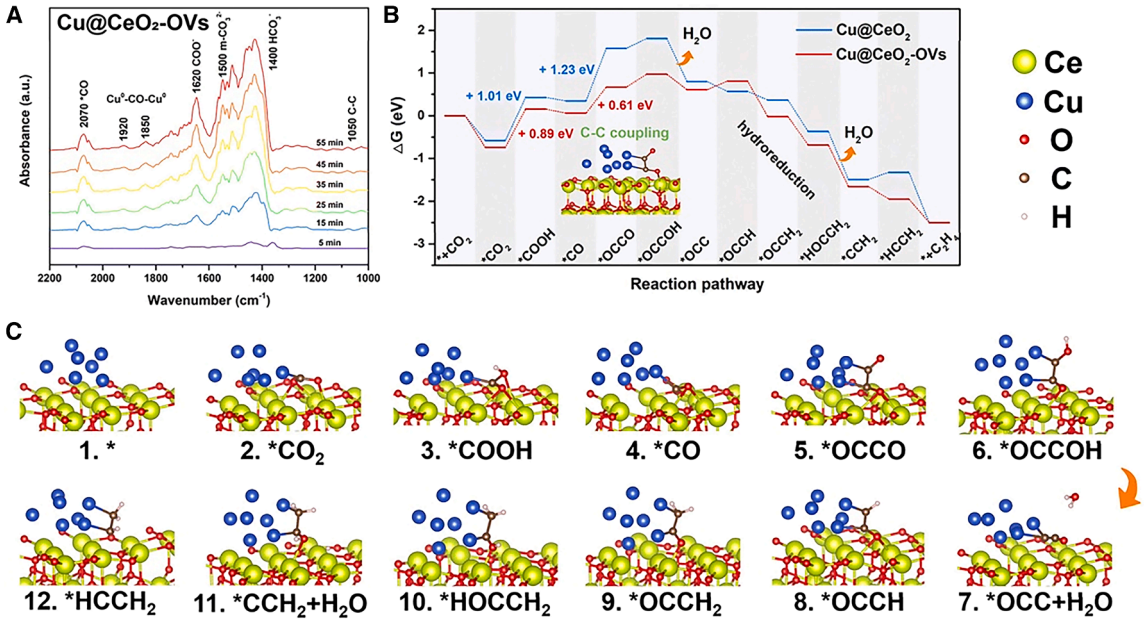

Figure 11. DFT results for the pathway from CO_2 to C_2H_4 over Cu@CeO_2-V_O''

(A) FTIR results.

(B) Minimum energy pathway from CO_2 to CO and C_2H_4 formation.

(C) Structural evolution of key intermediates along the CO_2-to-C_2H_4 conversion pathway over Cu@CeO_2–V_O''.

Reprinted with permission from Liu et al.[17] Copyright 2025 Royal Society of Chemistry.

Please cite this article in press as: Sasaki et al., Density functional theory-guided C–C coupling pathways in photocatalytic CO_2 reduction to C_2–C_3 products, Chem Catalysis (2026), https://doi.org/10.1016/j.checat.2026.101846

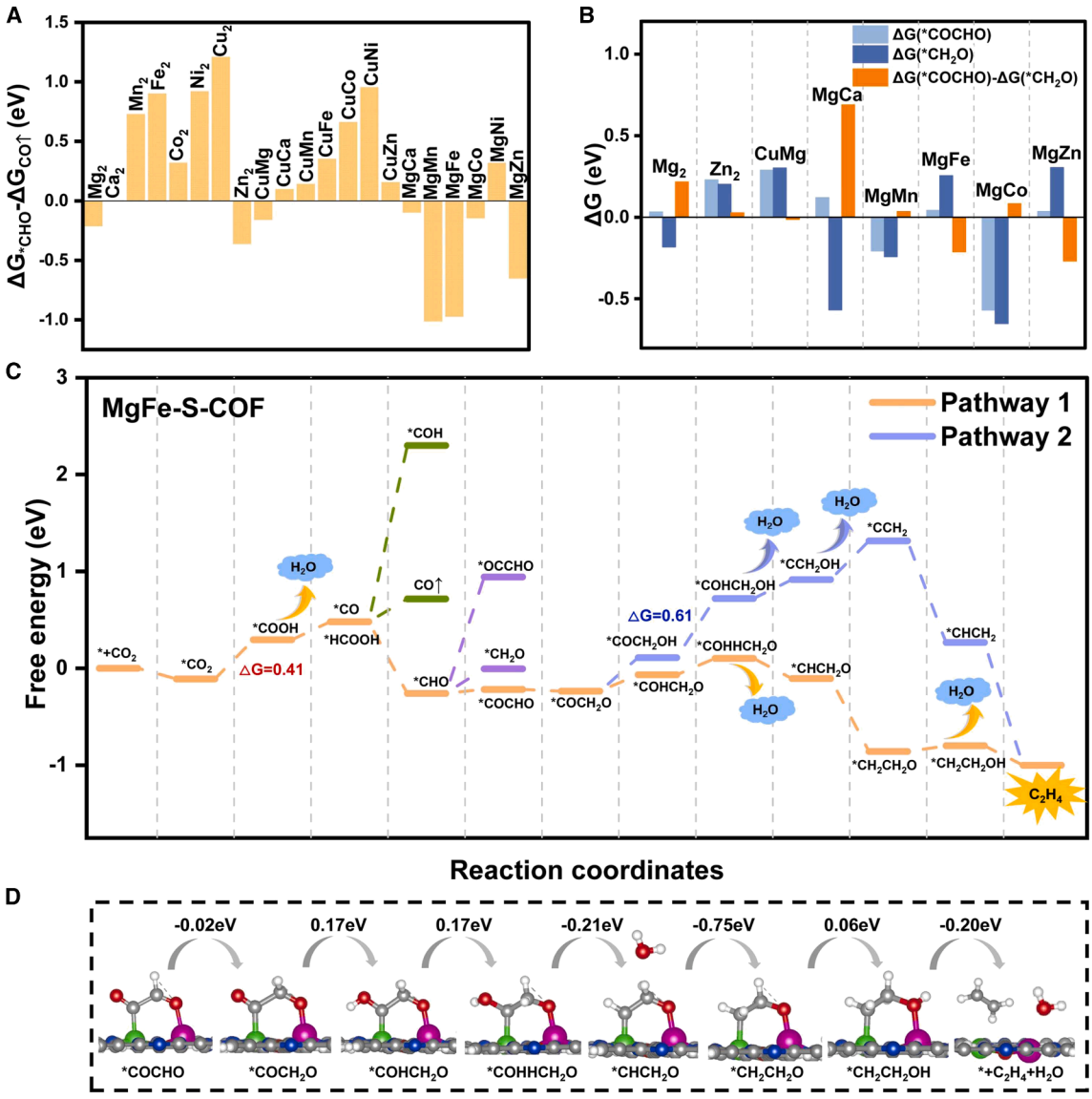

Figure 12. DFT results for the pathway from CO_2 to C_2H_4 over M–M′–COFs

(A) $\Delta_r G(CHO) - \Delta_r G(CO)$ (eV) values for M–M′–COFs

(B) $\Delta_r G(OC–CHO) - \Delta_r G(CH_2O)$ values for M–M′–COFs.

(C) Free energy diagrams for CO_2 reduction to C_2H_4 (orange lines) on Mg–Fe–COF.

(D) Optimized configurations of corresponding intermediates in C–C coupling to C_2H_4 on Mg–Fe–COF. Color key: purple, Mg; green, Fe; gray, C; red, O; blue, N; and white, H.

Reprinted from Zhang et al.[18] Copyright 2025 Elsevier.

intermediates"). E_{act} value for the following dissociative step to CO + OH species ("pathways from OCOH to CO") was only 0.02 eV, demonstrating favorable path rather than the associative hydrogenation step to HCO_2H. The following step from CO to CHO ("COH and/or CHO intermediates") was rate determining (E_{act} = 1.10 eV) to CH_3OH and/or CH_4 (Figure 18A; "CH_3 intermediates"). Compared with CH_3OH and CH_4 formation, associative HCO_2H formation from OCOH species required smaller E_{act} of 0.29 eV, suggesting higher selectivity toward HCO_2H.

As for the pathways to C_2 compounds, CHO–CHO coupling ("CHO–CHO coupling") was favored over CO–CO coupling ("CO–CO coupling" and "CO–CO coupling") and CO–CHO ("CO–CHO coupling" and "CO–CHO coupling"). However, the step from CO to CHO (1.10 eV) prior to the coupling was energetically disadvantageous compared with HCO_2H formation.[28]

Effects of solvents and competing adsorbents

Over the same single-atom Co–BP photocatalyst as in section "DFT approaches to photocatalysis-specific factors," AIMD

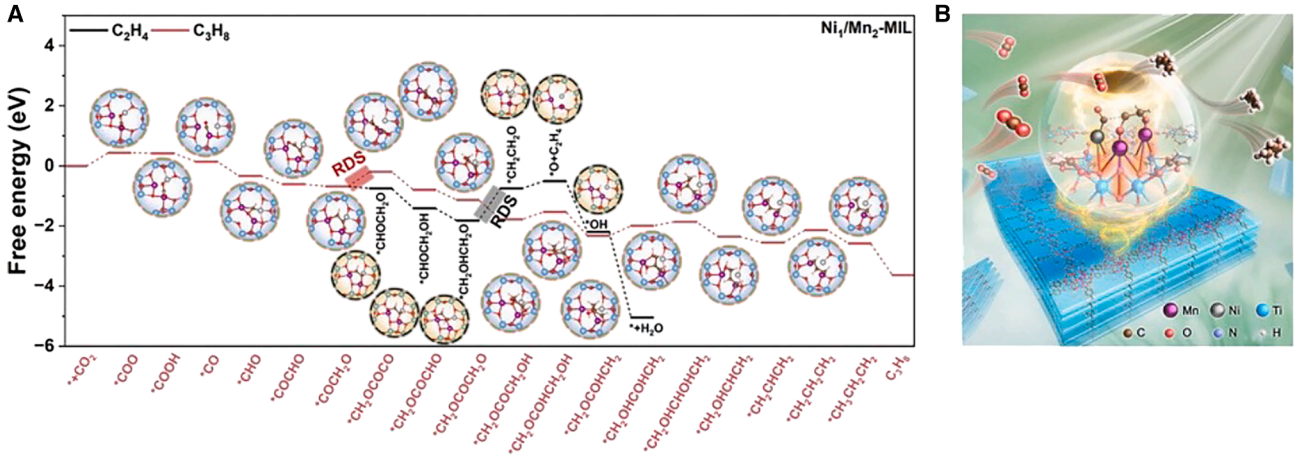

Figure 13. Free energy diagrams for photocatalytic CO_2 reduction to C_2H_4/C_3H_8 on $NiMn_2$–MIL

(A) Blue and yellow conformations represent intermediates in the C_3H_8 and C_2H_4 pathways, respectively. Color key: C, brown; O, red; Ti, blue; H, pink; N, bluish purple; Ni, gray; and Mn, purple.

(B) Schematic of photocatalytic CO_2 reduction to C_3H_8 on Ni_1/Mn_2–MIL.

Reprinted with permission from Wu et al.[19] Copyright 2026 Wiley-VCH.

analysis of reaction pathway was also performed in the mixed solvent of H_2O and acetonitrile. Surprisingly, the E_{act} value for the step from CO to CHO was reduced from 1.10 to 0.05 eV (Figures 18A–18D) owing to the stabilization by hydrogen bond, demonstrating that CHO was favored in realistic photocatalytic reaction conditions. Such formed CHO was able to move in the hydrogen bond network and had a possibility to couple with the other CHO in the medium.

The excited-state dynamics during CHO–CHO coupling step were analyzed by time-dependent (TD)-DFT/MD calculations

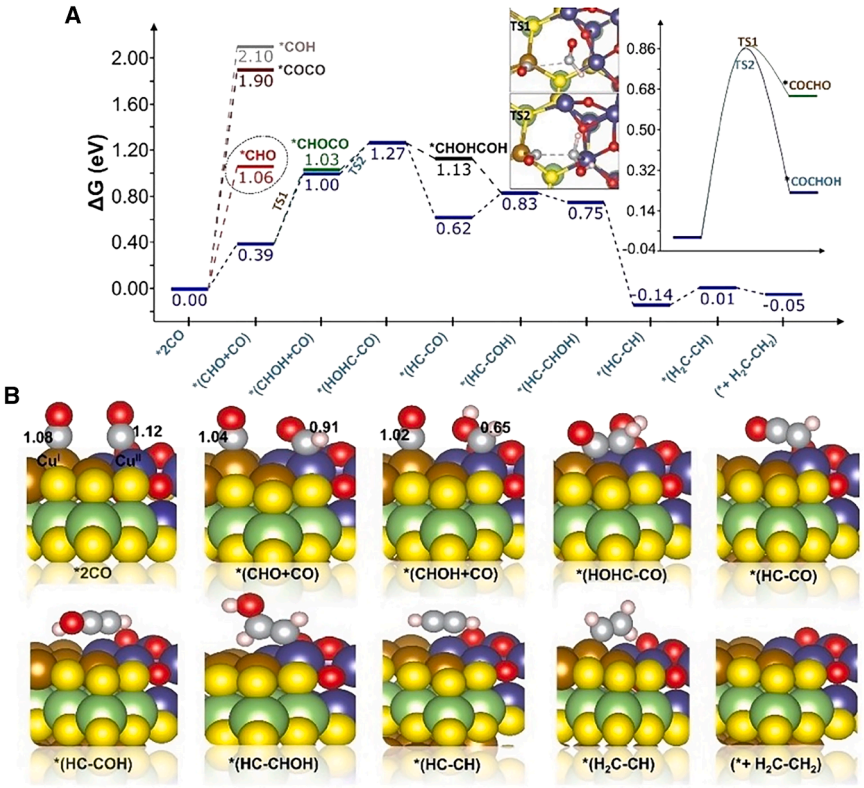

Figure 14. Proposed reaction pathway from CO_2 to C_2H_4

(A) Gibbs energy for CO reduction to C_2H_4 over $CuGaS_2$@CuO. Insets show the corresponding optimized transition-state geometry and profile for OC–CHO (red lines) and OC–CHOH (blue lines) coupling; the dashed circle represents the profile for hydrogenation of $CO@Cu^I$.

(B) Optimized geometry of intermediates on the catalyst surface via the minimum energy pathway. Numbers on C atoms show Bader charge distribution. S, yellow; Ga, green; Cu^I, brown; Cu^{II}, blue; O, red; C, gray; and H, white.

Reprinted with permission from Chakraborty et al.[20] Copyright 2023 Wiley-VCH.

Please cite this article in press as: Sasaki et al., Density functional theory-guided C–C coupling pathways in photocatalytic CO_2 reduction to C_2–C_3 products, Chem Catalysis (2026), https://doi.org/10.1016/j.checat.2026.101846

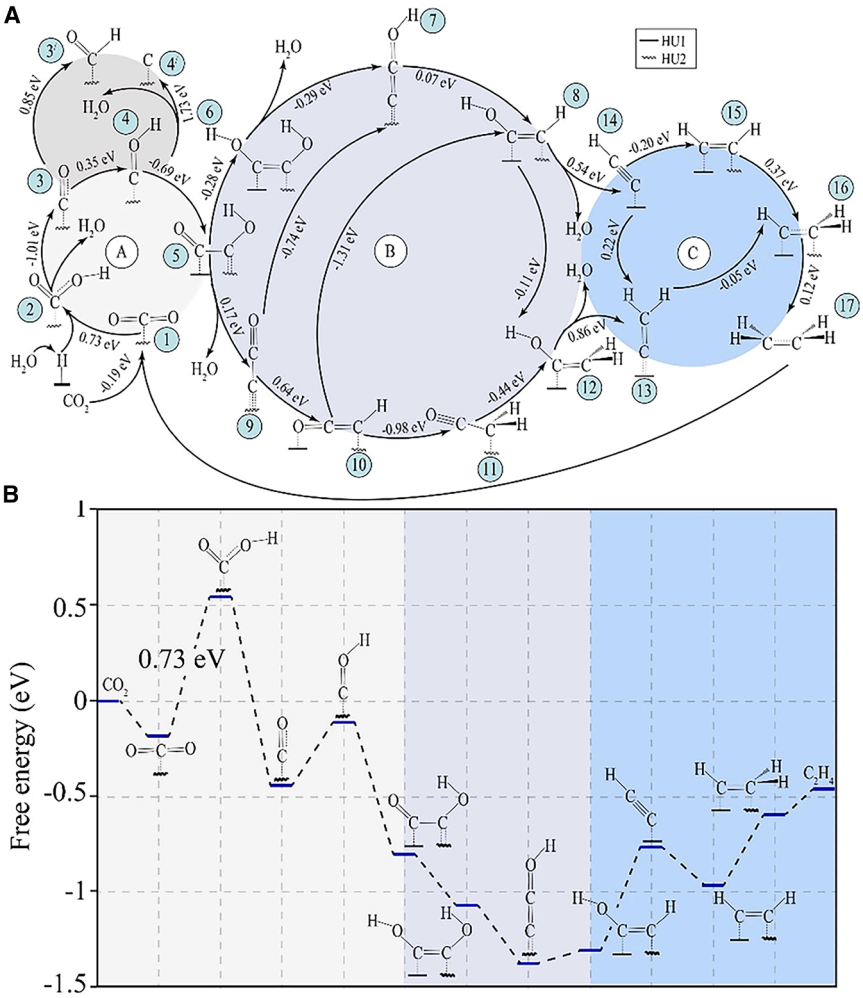

Figure 15. DFT analysis of reaction pathway from CO_2-to-C_2H_4 conversion

(A) All plausible pathways for C_2H_4 formation with corresponding free energy changes between intermediates. The conversion is expressed in three segments—A (OC–COH formation), B (O atom removal), and C (C_2H_4 formation from C≡CH)—where H in segment A derives from H_2O splitting. (B) Energy diagram for the most favorable C_2H_4 formation pathway on the $In_{2.77}S_4$–POP surface. Reprinted with permission from Das et al.[21] Copyright (2023) American Chemical Society.

based on *ab initio* real-time TD-DFT. As a result, time-dependent charge transfer and redistribution from the active site to surface species occurred through the support and/or solvent (Figure 19).

In summary, the reaction barrier can be changed owing to the charge transfer originating from the excitation by light, and the theoretical approach considering the excited state dynamics can explain specific reaction pathway of photocatalysis. In fact, Bader charge analysis,[9,10,25] differential analysis of charge density,[9,10,19,22,26,27] and NAMD and/or AIMD analysis[10] were also reported.

pH is essential for the photocatalysis in aqueous suspensions because the reaction pathways would vary: in the case of H_2O oxidation, dehydrogenation of H_2O (Equation 6) and oxidation of OH^- (Equation 7) proceed under acidic and basic conditions, respectively.

$$2H_2O + 4h^+ \rightarrow 4H^+ + O_2 \quad \text{(Equation 6)}$$

$$4OH^- + 4h^+ \rightarrow 2H_2O + O_2 \quad \text{(Equation 7)}$$

Over $BiVO_4$ photocatalyst, predominant species at the interface at each pH and adjusted band gap under aqueous solution were evaluated by MD simulation, and the reaction pathways were proposed dependent on the pH.[32,33] As a result, the reaction pathway based on Equation 6 was prevalent, while that based on Equation 7 was applicable only under strongly basic conditions.

The effects of competing adsorbent are often critical to determine the reaction pathways in photocatalysis. Adsorption of CO over Co nanoparticle (adsorption energy = −2.23 V) was remarkably weakened by the competing H adsorption (adsorption energy of CO = 1.36 eV), directing the reaction pathway from CO to C_2H_4 in the initial stage of photocatalysis to CH_4.[13]

Cu is one of the most frequently used for electrochemical/photocatalytic CO_2 reduction.[8,12,16,17,20,23,24,34] Over the Cu (1 1 1) surface, the effects of competing H adsorption and the competition with H_2-evolving reaction versus CO formation were evaluated.[34]

In fact, the reaction pathway from adsorbed CO_2 to OCOH, then CO + H_2O, was followed at the H coverage (θ_H) between 0 and 2/3 over Cu (1 1 1) surface (Figure 20A). The step from adsorbed CO_2 to OCOH species was preferred via Eley-Rideal mechanism with a proton-electron coupled transfer

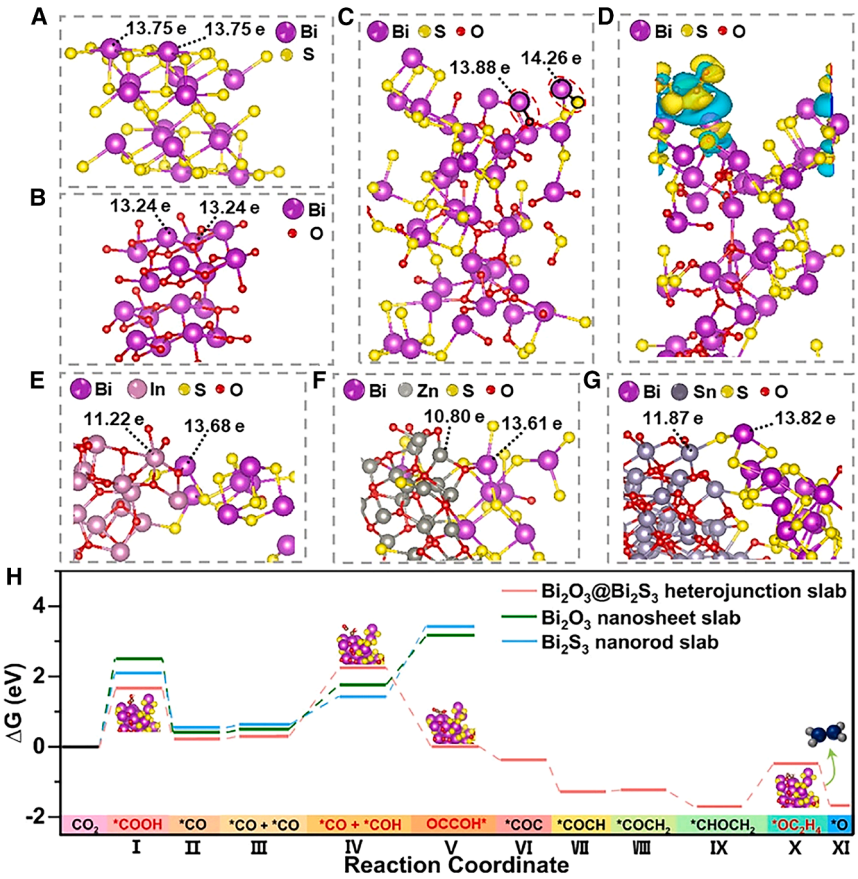

Figure 16. DFT calculations

(A–C) Calculated Bader charge values for (A) Bi_2O_3 nanosheet, (B) Bi_2S_3 nanorod, and (C) Bi_2O_3@Bi_2S_3 heterojunction.

(D) Charge density map for the OC–COH intermediate adsorbed on the Bi_2O_3@Bi_2S_3 heterojunction.

(E–G) Calculated Bader charge values for (E) In_2O_3@Bi_2S_3, (F) ZnO@Bi_2S_3, and (G) SnO_2@Bi_2S_3 heterojunctions.

(H) Free energy diagrams of CO_2 photoreduction to C_2H_4 over Bi_2O_3 nanosheet, Bi_2S_3 nanorod, and Bi_2O_3@Bi_2S_3 heterojunction.

Reprinted with permission from Zhang et al.[22] Copyright 2025 American Chemical Society.

to adsorbed CO_2. The E_{act} value increased from 0.35 eV (θ_H = 0) to 0.96 eV (θ_H = 2/3). E_{act} value for the step from OCOH to CO was ~0.10 eV and exergonic to form CO (Figure 20A).

In comparison, more favorable pathway to $HCOO^-$ was demonstrated via Langmuir-Hinshelwood mechanism, with E_{act} = 0.15 eV at θ_H = 0. In the θ_H dependence, E_{act} value also increased to 0.60 eV at θ_H = 2/3 (Figure 20B). It was important to theoretically predict the favorable mechanism over the catalyst surface as well as the effects of competitive adsorption depending on the reaction conditions, e.g., pH.

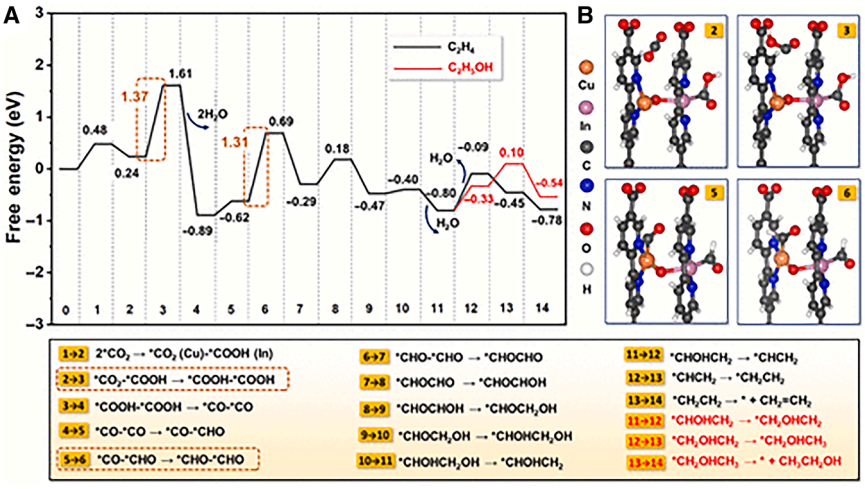

Scheme 7. Reaction pathway from CO_2 to C_2-compounds using Cu-In/Ti-BPDC

(A) Calculated Gibbs free energy diagram of the optimal CO_2-to-C_2 (C_2H_5OH and C_2H_4) reduction pathway on Cu–In/Ti–BPDC.

(B) Optimized structures of all states involved in high-free-energy-change steps (2 → 3 and 5 → 6).

Reprinted with permission from Wang et al.[23] Copyright 2025 Chinese Chemical Society.

Please cite this article in press as: Sasaki et al., Density functional theory-guided C–C coupling pathways in photocatalytic CO_2 reduction to C_2–C_3 products, Chem Catalysis (2026), https://doi.org/10.1016/j.checat.2026.101846

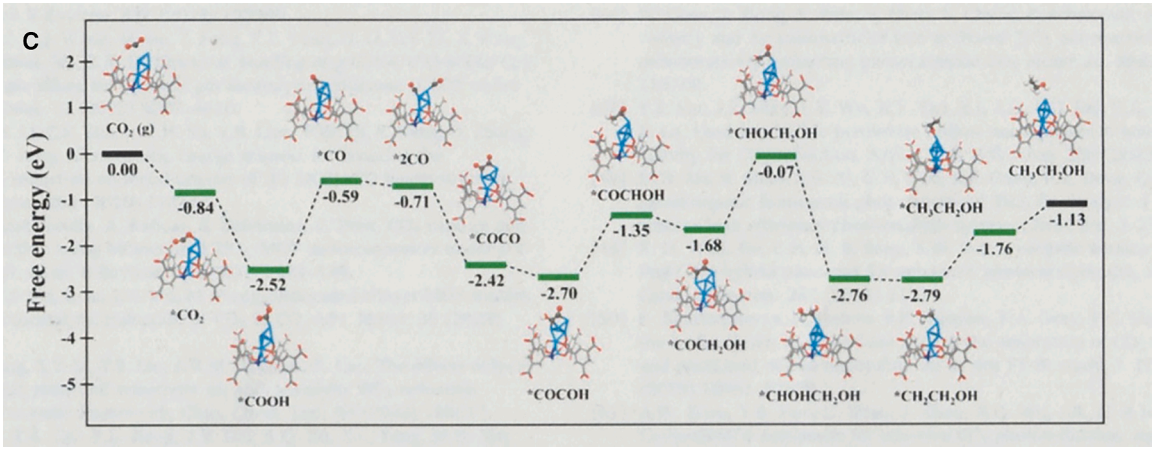

Scheme 8. Free energy diagram and optimized intermediate structures for CO_2 photoreduction using Cu–NH_2–BDC@TiO_2
Reprinted from Xia et al.[24] Copyright 2024 Elsevier.

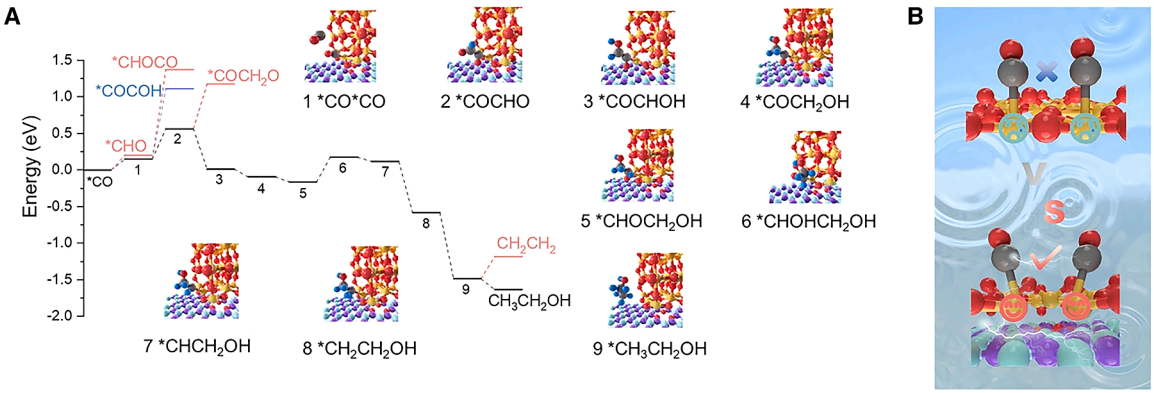

Figure 17. Theoretical simulation of CO_2 reduction to C_2H_5OH
(A) Reaction energy profiles and corresponding intermediate structures for C_2H_5OH formation via CO_2 reduction on TiO_{2-x}/BN.
(B) Mechanism of S-scheme heterojunction and $V_O^{\cdot\cdot}$.
Reprinted with permission from Liu et al.[25] Copyright 2026 Wiley-VCH.

The required energies (overpotential if we assume electrochemical reduction of CO_2) to CO and H_2 were also plotted depending on surface coverage of θ_H and θ_{CO}, respectively (Figure 21).[34] H_2 evolution reaction required lower energy in the range of θ_H = 0.1–0.8 compared with that in the range of θ_{CO} = 0.1–0.8; H_2 evolution occurs more facile in a wide range of reaction conditions.

Furthermore, the preferable C_2 formation was evaluated compared with C_1 and H_2 formations using Cu–Zn and Cu–Ag alloy nanoparticles.[35] Based on $\Delta_r G$ values as in Equation 8,

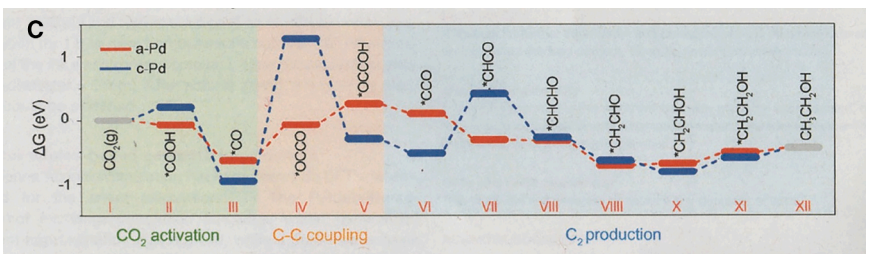

Scheme 9. Free energy diagram for reaction pathways from CO_2 to C_2H_5OH on amorphous and crystalline Pd supported on $Cd_{0.9}Zn_{0.1}S$ nanorods
Reprinted from Tan et al.[26] Copyright 2025 Elsevier.

Please cite this article in press as: Sasaki et al., Density functional theory-guided C–C coupling pathways in photocatalytic CO_2 reduction to C_2–C_3 products, Chem Catalysis (2026), https://doi.org/10.1016/j.checat.2026.101846

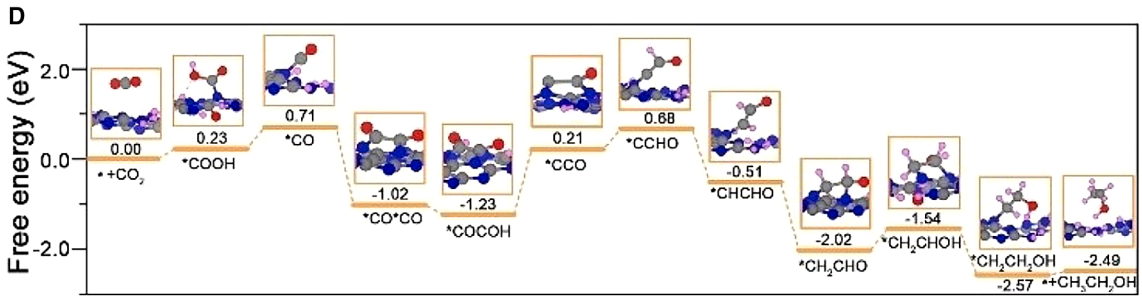

Scheme 10. Free energy diagram of photocatalytic CO_2 reduction and intermediate adsorption model of O-doped, N-defective organic compound

Reprinted with permission from Tan et al.[27] Copyright 2025 Wiley-VCH.

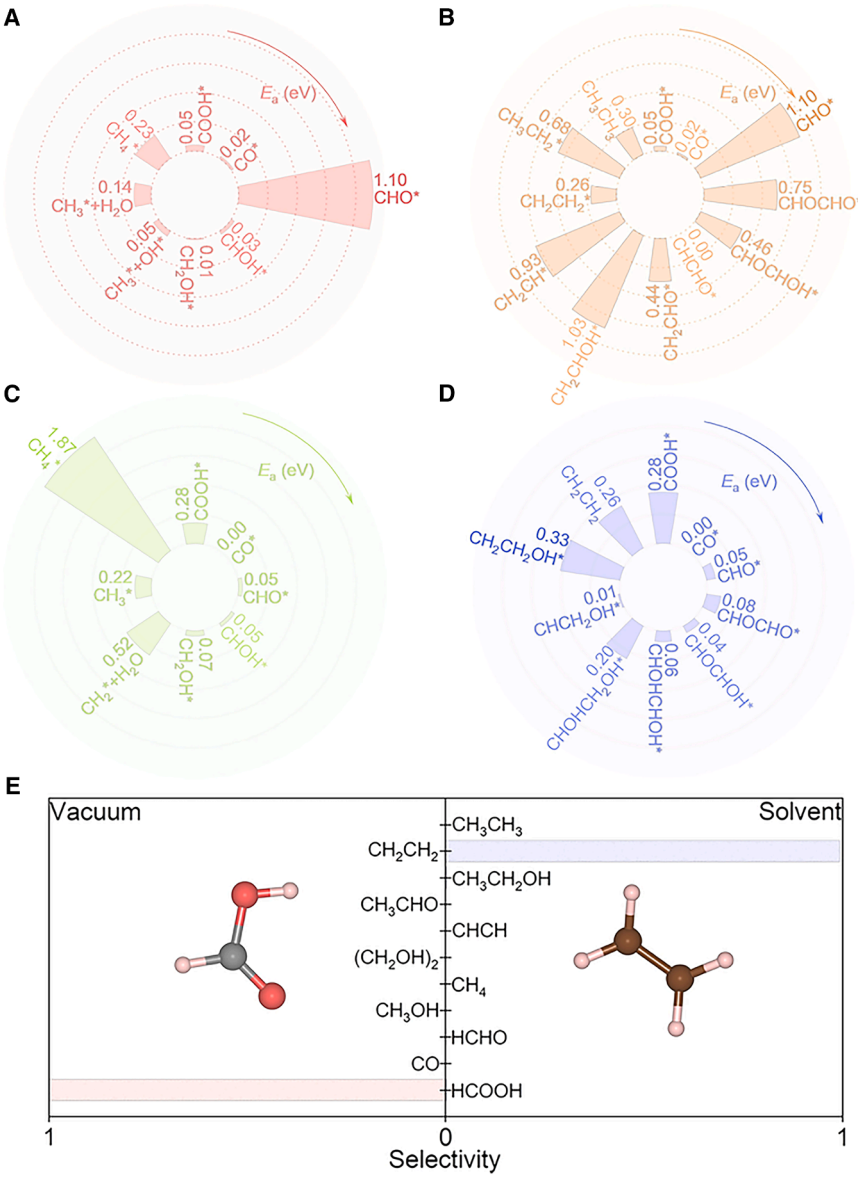

Figure 18. Reaction pathway from CO_2 to C_1–C_2 products over Co–BP

(A–D) Reaction barriers for (A) CH_4 and (B) C_2H_6 formation under gas and (C) CH_4 and (D) C_2H_4 formation under solvent.

(E) Product selectivity under gas and solvent.

Reprinted with permission from Sun et al.[28] Copyright 2025 Wiley-VCH.

Please cite this article in press as: Sasaki et al., Density functional theory-guided C–C coupling pathways in photocatalytic CO_2 reduction to C_2–C_3 products, Chem Catalysis (2026), https://doi.org/10.1016/j.checat.2026.101846

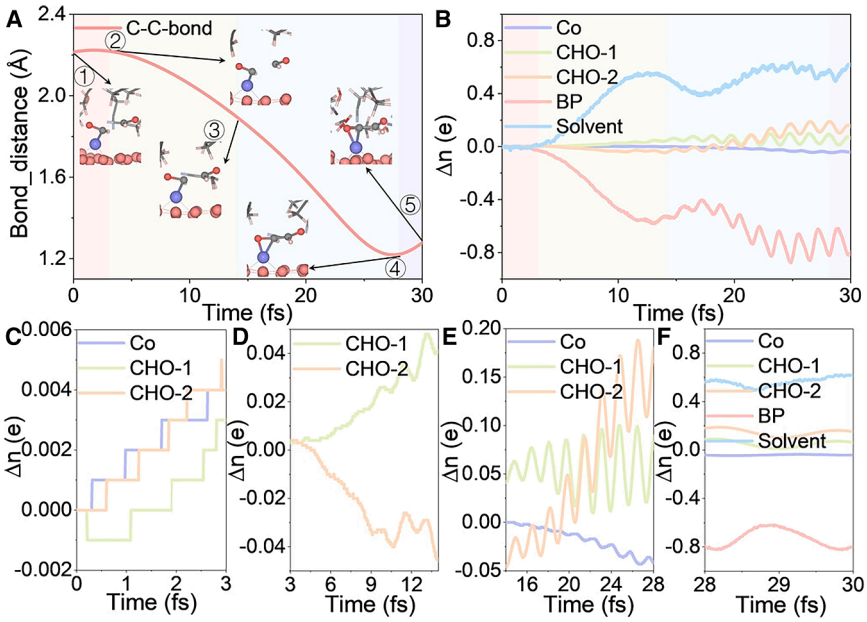

Figure 19. Time-dependent DFT/MD calculation results over Co–BP

(A) The bond length of C−C on the Co–black P evolves with time at light. Snapshots at three representative times (0, 3, 14, 28, and 30 fs) during the CHO couple process on Co–BP are shown in insets 1–5.

(B) Time evolution of electron populations for the species in the period of 0–30 fs under the irradiation of light.

(C–F) Piecewise temporal evolution of electron populations under the irradiation of light. The adsorbed CHO on the Co atom is labeled CHO-1, and the free CHO specie is labeled CHO-2.

Reprinted with permission from Sun et al.[28] Copyright 2025 Wiley-VCH.

$$\Delta_r G = \Delta_r H - T\Delta_r S + \text{zero point energy} - eU \quad \text{(Equation 8)}$$

in which H, S, T, and U are enthalpy, entropy, temperature, and electric potential, respectively. The dimerization of adsorbed CO was favored over hydrogenation of CO to CHO (Figures 22A and 22B). Whether H adsorption energy $\Delta_r G_H$ is less than and more than zero, H_2 and $C_{1/2}$ compound formations were preferred, respectively, while when limiting potential, U_L was smaller than $\Delta_r G_H$, and H poisoning should be serious rather than spontaneous H_2 formation. One concern in the work by Iqbal et al.[35] is that U_L value is limited for C–C coupling and CO + H steps and the other steps of greater $\Delta_r G$ are not well checked, e.g., from CHCHO to CH_2CHO species.

SUMMARY AND OUTLOOK

Summary

Recent advances in CO_2 photoconversion pathways have been surveyed. Classical H_2CO and carbene pathways (Scheme 1) provide several plausible reaction steps. Notably, the initial hydrogenation of CO_2 to OCOH has frequently been identified as the rate determining and/or thermodynamic potential determining. Both pathways have become obsolete as the key OCOH decomposition step to CO (Table 1, rows c, d, and t) was not described in these pathways.

Later than the rate-determining and/or thermodynamic potential-determining steps, hydrogenation at C atom (Table 1, rows a, c', f, and f') can be regarded as a variation of the latter steps of the carbene pathway (Scheme 1, right), whereas hydrogenation at the O atom (Table 1, rows p and r) corresponds to variations of the latter steps of the H_2CO pathway (Scheme 1, left).

Recent advances also extend to the photocatalytic products beyond those described by the H_2CO and carbene pathways established in 2016. A key step is CO–CO coupling,[11,14–17,24–27] forming C_2H_4 and/or C_2H_6 in the gas phase or C_2H_5OH in aqueous medium, where this step is rate determining and/or thermodynamic potential determining. A common feature of photocatalysts that proceed via CO–CO coupling is the presence of two neighboring active metal sites. In electrochemical CO_2 reduction, CO–CO coupling leading to C_2H_4 has also been supported.[36]

Other C–C coupling types reported include CO_2–CO_2,[10] CO–CHO,[12,18,19] CH_3–CH_3,[13] CO–CHOH,[20] CO–COH,[21,22] and CHO–CHO.[23] Generalizing the energetic difference among these pathways is difficult as the outcome likely varies with computational methodology. When verifying the reaction pathways on a catalyst surface, it is essential to identify the saddle points along the reaction coordinate, for example, a change in the first derivative $\frac{dG}{d\xi}$ from positive to negative or a second derivative $\frac{d^2G}{d\xi^2} \leq 0$, and determine the minimum-energy path, for example, via CI-NEB. This is because even if a reaction is considered exergonic based on $\Delta_r G$ values, the reaction pathway cannot be properly rationalized if the energy barrier to reach the transition state is sufficiently high. Pathways predicted from $\Delta_r G$ alone apply only the criterion of spontaneous change (negative $\Delta_r G$) at equilibrium.

Technical possibilities and prospects

Gibbs energy is correlated with the equilibrium constant K as

$$\Delta_r G^{\ominus} = -RT \ln K, \quad \text{(Equation 9)}$$

where R is the gas constant. Molar partition function q_m can be expressed as

$$G(T) = G(0) - nRT \ln \frac{q_m}{N_A}, \quad \text{(Equation 10)}$$

where n is amount of substance, and N_A is Avogadro's number. Accordingly, equilibrium constant K for the reaction aA + bB → cC + dD can be expressed with standard molar partition functions as

Please cite this article in press as: Sasaki et al., Density functional theory-guided C–C coupling pathways in photocatalytic CO_2 reduction to C_2–C_3 products, Chem Catalysis (2026), https://doi.org/10.1016/j.checat.2026.101846

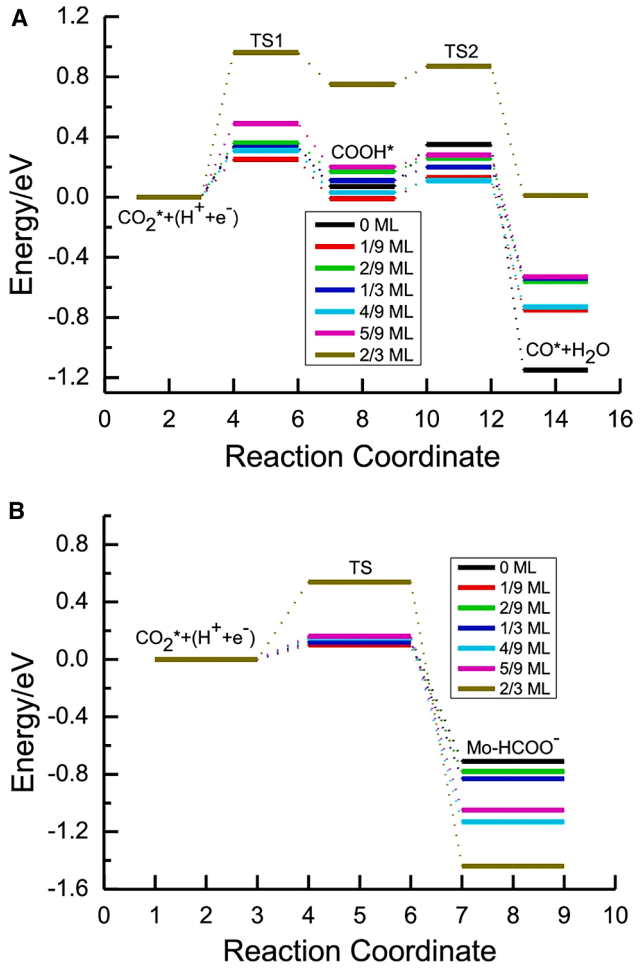

Figure 20. Reaction pathways from CO_2 to CO/$HCOO^-$ over Cu (1 1 1) surface

Calculated energy diagrams of CO_2 reduction to (A) CO through OCOH intermediate at different H coverages via the Eley-Rideal mechanism and (B) monodentate $HCOO^-$ species at different H coverages via the Langmuir-Hinshelwood mechanism. Reprinted with permission from Ou and He.[34] Copyright 2020 American Chemical Society.

$$K = \frac{\left(q^{\ominus}_{C,m}/N_A\right)^c \left(q^{\ominus}_{D,m}/N_A\right)^d}{\left(q^{\ominus}_{A,m}/N_A\right)^a \left(q^{\ominus}_{B,m}/N_A\right)^b} e^{-\frac{\Delta_r E_0}{RT}}. \quad \text{(Equation 11)}$$

Similarly, equilibrium constant K for the reaction A + B → activated complex $C^{\ddagger}$ can be expressed as

$$K^{\ddagger} = \frac{q^{\ominus}_{C^{\ddagger},m}}{q^{\ominus}_{A,m} q^{\ominus}_{B,m}} \frac{N_A}{} e^{-\frac{\Delta E_0}{RT}}. \quad \text{(Equation 12)}$$

The partition function q for the vibration mode to pass through the transition state in the activated complex $C^{\ddagger}$ is

$$q = \frac{1}{1 - e^{-\frac{h\nu^{\ddagger}}{kT}}} \simeq \frac{1}{1 - \left(1 - \frac{h\nu^{\ddagger}}{kT}\right)} = \frac{kT}{h\nu^{\ddagger}} \ (\nu^{\ddagger} \simeq 0). \quad \text{(Equation 13)}$$

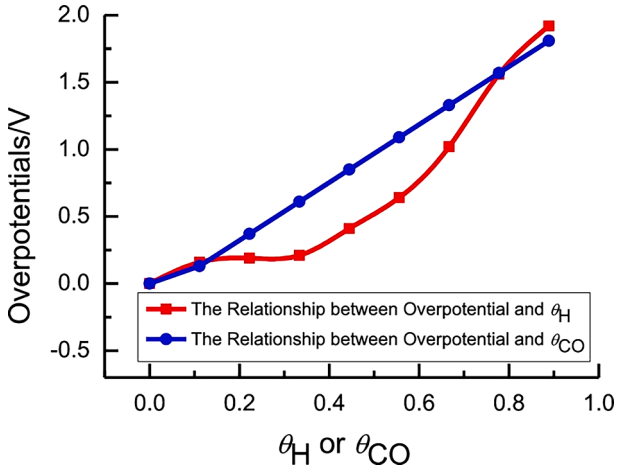

Figure 21. Obtained relationships between overpotentials and θ_H and θ_{CO} based on H and CO coverage-dependent electrochemical model

Reprinted with permission from Ou and He.[34] Copyright 2020 American Chemical Society.

If we assume partition function $\overline{q}^{\ddagger}_C$ for all the other modes of activated complex $C^{\ddagger}$,

$$q^{\ominus}_{C^{\ddagger},m} = \frac{kT}{h\nu^{\ddagger}} \overline{q}^{\ddagger\ominus}_C. \quad \text{(Equation 14)}$$

When we substitute Equation 14 into Equation 12,

$$K^{\ddagger} = \frac{kT}{h\nu^{\ddagger}} \frac{N_A \overline{q}^{\ddagger\ominus}_C}{q^{\ominus}_{A,m} q^{\ominus}_{B,m}} e^{-\frac{\Delta E_0}{RT}}. \quad \text{(Equation 15)}$$

The equilibrium of A + B → $C^{\ddagger}$ can be also expressed with activities a and then partial pressures of each species as

$$K^{\ddagger} = \frac{a^{\ddagger}_C}{a_A a_B} = \frac{p^{\ddagger}_C/p^{\ominus}}{(p_A/p^{\ominus})(p_B/p^{\ominus})} = \frac{p^{\ddagger}_C\, p^{\ominus}}{p_A p_B}. \quad \text{(Equation 16)}$$

Furthermore, partial pressure p_J is expressed with molar concentration [J] as

$$p_J = RT\,[J]. \quad \text{(Equation 17)}$$

When we substitute Equation 17 into Equation 16,

$$K^{\ddagger} = \frac{[C^{\ddagger}]\, p^{\ominus}}{RT\,[A][B]}. \quad \text{(Equation 18)}$$

The decomposition rate of activated complex $C^{\ddagger}$ to product is

$$\text{rate} = k^{\ddagger}[C^{\ddagger}] = \frac{RT}{p^{\ominus}} k^{\ddagger} K^{\ddagger}[A][B]. \quad \text{(Equation 19)}$$

The rate constant $k^{\ddagger}$ is regarded as proportional to $\nu^{\ddagger}$,

$$k^{\ddagger} = \kappa\nu^{\ddagger}, \quad \text{(Equation 20)}$$

where κ is transmission coefficient. When we substitute Equations 15 and 20 into Equation 19,

Please cite this article in press as: Sasaki et al., Density functional theory-guided C–C coupling pathways in photocatalytic CO_2 reduction to C_2–C_3 products, Chem Catalysis (2026), https://doi.org/10.1016/j.checat.2026.101846

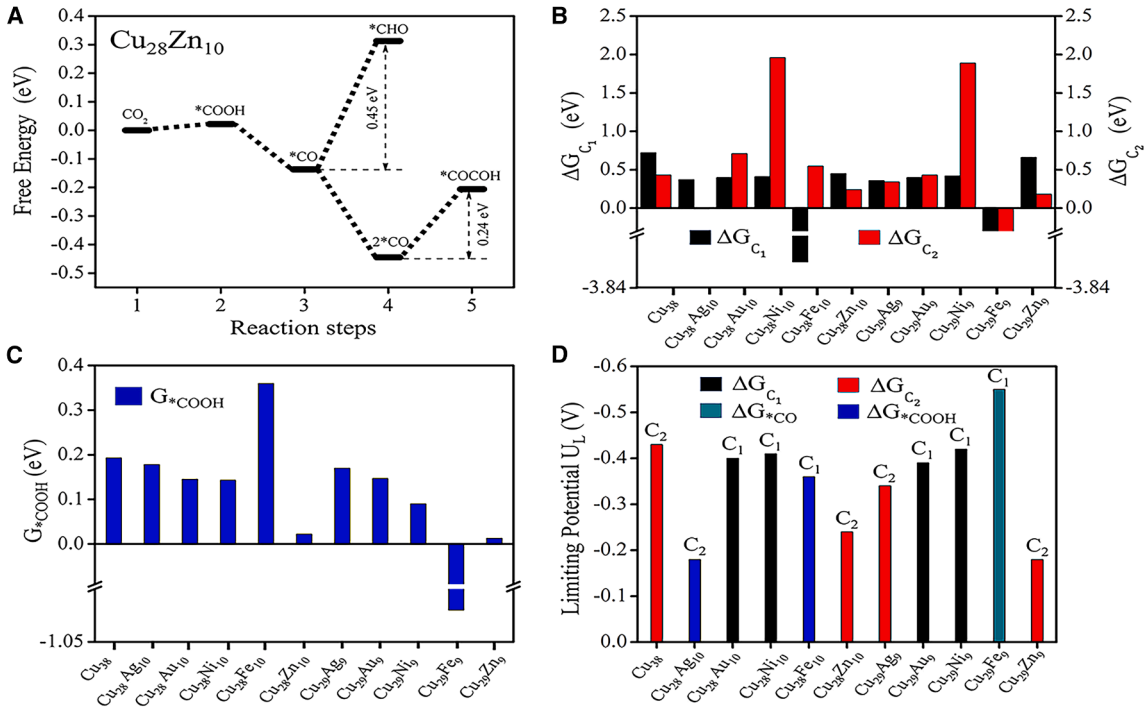

Figure 22. Reaction pathway from CO_2 to C_1–C_2 products over $Cu_{28}Zn_{10}$ and the other alloys

(A) Energy profile representing the first four steps toward CO_2 reduction through the C_1 and C_2 pathways on the $Cu_{28}Zn_{10}$ catalyst.

(B) Free energy change ΔG_{C1} and ΔG_{C2} for various Cu_{38}-based alloy catalysts.

(C) Energy change ΔG_{COOH} on various Cu_{38}-based alloy catalysts.

(D) U_L during CO_2 reduction on various Cu_{38}-based alloy catalysts.

Reprinted with permission from Iqbal et al.[35] Copyright 2024 American Chemical Society.

$$\text{rate} = k_r[A][B], k_r \equiv \kappa \frac{kT}{h}\frac{RT}{p^{\ominus}}\frac{N_A \overline{q}_C^{\ddagger\ominus}}{q_{A,m}^{\ominus} q_{B,m}^{\ominus}} e^{-\frac{\Delta E_0}{RT}}, \quad \text{(Equation 21)}$$

Based on Equations 20 and 21,

$$\nu_r \equiv \frac{kT}{h}\frac{RT}{p^{\ominus}}\frac{N_A \overline{q}_C^{\ddagger\ominus}}{q_{A,m}^{\ominus} q_{B,m}^{\ominus}} e^{-\frac{\Delta E_0}{RT}}. \quad \text{(Equation 22)}$$

Based on Equation 22, the frequency of surpassing the saddle point is expressed as follows:

$$\nu = \nu_0 \exp\left(-\frac{E_{act}}{RT}\right). \quad \text{(Equation 23)}$$

To obtain E_{act}, the NEB method constructs images of the initial and final states with multiple intermediate images at constant intervals. Then, springs are added between images and equalized on both sides of the pathway and set to zero in the vertical direction to calculate the lowest energy path.

CI-NEB is the revised version. It first determines the highest energy image along the path as the transition-state candidate. For this image, the spring forces maintaining the interval with adjacent images are disabled, and a new force is applied to maximize the energy along the path direction. Owing to this procedure, the specific image "climbs" to the true saddle point, that is, the transition state. This method enables more accurate determination of saddle points and provides information on the minimum-energy path without a substantial increase in computational cost as it evaluates images at fixed intervals.[37,38] Other saddle-point search methods include the dimer method and the activation-relaxation technique nouveau (ARTn).

The dimer method locates a saddle point on a potential energy surface from a single starting point, performing calculations for two images—the initial state and a rotated point around the saddle point—without requiring the final state.[39]

In contrast, the ARTn method transitions from a local energy minimum in a random direction, while minimizing total energy to search for saddle points.[40] Both methods share the advantage of not requiring a final state. However, ARTn generally outperforms the dimer method for systems with greater degrees of freedom and/or when searching for multiple saddle points.

As an example of the application of dimer method, the CO_2 photoreduction pathway was effectively pursued over Pd (1 1 1) surface in combination with CI-NEB method.[41] In the study, the initial transition state structure was estimated using the CI-NEB method, and the initial reaction pathway was extended and converged to the saddle point of the rate-determining step. Such combinational approach of the advantages of CI-NEB and dimer methods is expected to pursue more accurate evaluation of reaction pathways.

The ARTn method has not fully been applied to find the CO_2 photoreduction pathway yet; however, the ARTn method was

Please cite this article in press as: Sasaki et al., Density functional theory-guided C–C coupling pathways in photocatalytic CO_2 reduction to C_2–C_3 products, Chem Catalysis (2026), https://doi.org/10.1016/j.checat.2026.101846

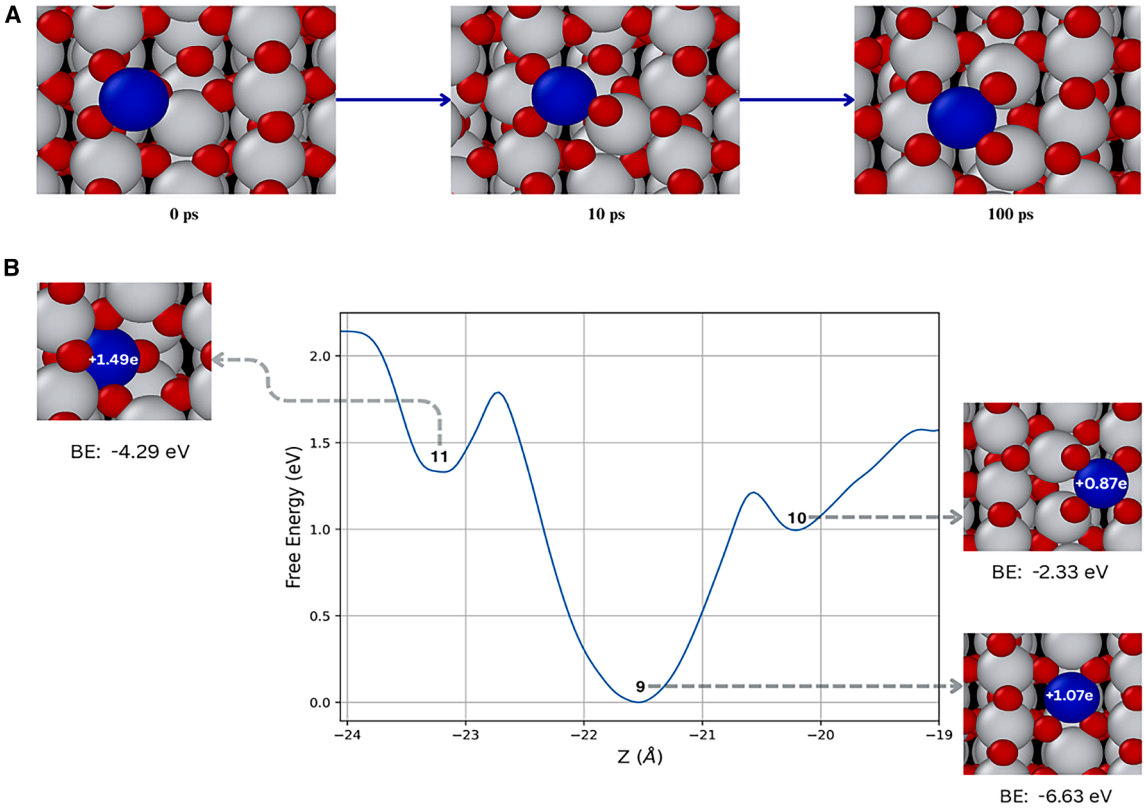

Figure 23. Computed results of Pt atom position over rutile-type TiO_2 (1 1 0) surface

(A) Formation of PtO_4 at 1,000 K where Pt atom is initiated near the $V_{Ti5c}^{\cdots}$ site.

(B) Well-tempered metadynamics-reconstructed free energy surface at 1,000 K. The Bader charges for the Pt motifs are highlighted along with the DFT computed binding energy.

Reprinted with permission from Saleem and Sharada.[46] Copyright 2026 Royal Society of Chemistry.

already utilized to evaluate the stability of $V_O^{\cdot\cdot}$ sites at a-TiO_2 (1 0 1) surface and their diffusion[42] and to simulate the diffusion of O atom and oxidation pathway over Pt (1 1 1) surface closely related to the CO_2 photoreduction reactivity.[43]

Furthermore, temperature dependence cannot be verified solely by these static methods. Even when the reaction pathways are inferred, molecular behavior remains difficult to determine. Metadynamics enables the simulation of molecular surface dynamics using MD and Monte Carlo methods,[44] offering results that correspond more closely to experimental data and accommodating large-scale systems at appropriate temperature and pressure.[45] Precise local structural calculations for reaction processes based on CI-NEB, dimer, and/or ARTn can, thus, be complemented by metadynamics.

The migration of single Pt atom over rutile-type TiO_2 (1 1 0) comprising $V_{Ti}^{\cdots\cdot}$ and/or $V_O^{\cdot\cdot}$ sites and the stability were evaluated using both static and dynamic methods at finite temperature.[46] As described insection "DFT approaches to photocatalysis-specific factors", while DFT can be combined with AIMD, AIMD demands heavy computational capacity and is limited to a few picoseconds (ps). In comparison, longer timescale well-tempered metadynamics employing machine learning interatomic potentials were employed. Then, based on Equation 23, rate constants k_r was obtained.

Based on the MD simulations utilizing machine learning interatomic potentials on nanosecond scale at 1,000 K, Pt atom around $V_O^{\cdot\cdot}$ site essentially remained at the $V_O^{\cdot\cdot}$ site. In clear contrast, Pt atom around $V_{Ti}^{\cdots\cdot}$ site restructured to square-planar PtO_4 on a 100 ps timescale (Figure 23A) over the potential surface of TiO_2 (1 1 0) surface.

Then, the CI-NEB method at 0 K and well-tempered metadynamics methods considering temperature evaluated the migration energy of Pt atom around the $V_O^{\cdot\cdot}$ and/or $V_{Ti}^{\cdots\cdot}$ sites. The migration energy around $V_{Ti}^{\cdots\cdot}$ site was 2.56 eV, as determined by the CI-NEB method; in contrast, the corresponding value obtained using the well-tempered metadynamics method at 1,000 K was 1.20 eV (Figure 23B). Thus, dynamics simulation assuming finite temperature is valuable to evaluate the temperature-dependent reaction barrier and the following reaction pathway to provide k_r value based on Equation 21.

For future work, the dimer and ARTn methods are promising for elucidating reaction pathways on catalytically complex surfaces, such as neighboring dual metal sites, because they efficiently search for unknown saddle points without

predefined final states. In particular, they potentially provide more detailed insights into the transition states in various C–C coupling processes, including the CO–CO, CO_2–CO_2, CO–CHO, CH_3–CH_3, CO–CHOH, CO–COH, and CHO–CHO couplings described in this review. Clarifying which coupling pathway is selected by specific dual metal site features on the photocatalyst surface represents a next key step for future investigations using these techniques.

Metadynamics, meanwhile, enables computations under conditions close to real experimental environments by incorporating temperature effects and accommodating larger molecular and atomic ensembles. This approach is also expected to describe real reaction pathways, favorable intermediate species, and the competition between C–C coupling and hydrogenation along the overall CO_2 photoreduction pathway.

ACKNOWLEDGMENTS

The authors are grateful for the financial support from the Grant-in-Aid for Scientific Research B (24K01522 and 20H02834 to Y.I.) from the Japan Society for the Promotion of Science. A part of the computation was performed using the facilities of the Institute for Solid State Physics, University of Tokyo (2025-Bb-0019 and 2024-Bb-0004). The authors would like to thank Enago (www.enago.jp) for the language review.

AUTHOR CONTRIBUTIONS

All authors have contributed to the writing of the manuscript.

DECLARATION OF INTERESTS

The authors declare no competing interests.

SUPPLEMENTAL INFORMATION

Supplemental information can be found online at https://doi.org/10.1016/j.checat.2026.101846.

REFERENCES

1. Izumi, Y. (2013). Recent advances in the photocatalytic conversion of carbon dioxide to fuels with water and/or hydrogen using solar energy and beyond. Coord. Chem. Rev. *257*, 171–186. https://doi.org/10.1016/j.ccr.2012.04.018.
2. Izumi, Y. (2015). Advances in CO_2 Capture, Sequestration, and Conversion, 1194 (ACS Publications). https://doi.org/10.1021/bk-2015-1194.
3. Ma, J., Miao, T.J., and Tang, J. (2022). Charge carrier dynamics and reaction intermediates in heterogeneous photocatalysis by time-resolved spectroscopies. Chem. Soc. Rev. *51*, 5777–5794. https://doi.org/10.1039/d1cs01164b.
4. Habisreutinger, S.N., Schmidt-Mende, L., and Stolarczyk, J.K. (2013). Photocatalytic reduction of CO_2 on TiO_2 and other semiconductors. Angew. Chem. Int. Ed. *52*, 7372–7408. https://doi.org/10.1002/anie.201207199.
5. Ji, Y., and Luo, Y. (2016). New mechanism for photocatalytic reduction of CO_2 on the anatase TiO_2 (1 0 1) surface: the essential role of oxygen vacancy. J. Am. Chem. Soc. *138*, 15896–15902. https://doi.org/10.1021/jacs.6b05695.
6. Ya, L., and Liejin, G. (2020). On factors limiting the performance of photoelectrochemical CO_2 reduction. J. Chem. Phys. *152*, 100901.
7. Ji, Y., and Luo, Y. (2016). Theoretical study on the mechanism of photoreduction of CO_2 to CH_4 on the anatase TiO_2 (1 0 1) surface. ACS Catal. *6*, 2018–2025. https://doi.org/10.1021/acscatal.5b02694.
8. Chen, H., Fan, T., and Ji, Y. (2023). CO_2 reduction mechanism on the Cu_2O (1 1 0) surface: A first-principles study. ChemPhysChem *24*, e202300047. https://doi.org/10.1002/cphc.202300047.
9. Hara, K., Nozaki, M., Hirayama, R., Ishii, R., Niki, K., and Izumi, Y. (2023). Adsorbed CO_2-mediated CO_2 photoconversion cycle into solar fuel at the O vacancy site of zirconium oxide. J. Phys. Chem. C *127*, 1776–1788. https://doi.org/10.1021/acs.jpcc.2c06048.
10. Sun, F.-l., Lin, C.-b., Zhang, W., Chen, Q., Chen, W.-x., Li, X.-n., and Zhuang, G.-l. (2023). Dual activation and C–C coupling on single atom catalyst for CO_2 photoreduction. npj Comput. Mater. *9*, 220. https://doi.org/10.1038/s41524-023-01177-3.
11. Duan, Y., Zhao, H., Ji, J., Shen, Z., Wang, Y., and Du, Y. (2025). Highly selective photocatalytic CO_2 reduction to C_2H_6 via nanocluster-single atom-vacancy on ceria: synergistic mechanism and orbital effects. Nano Lett. *25*, 6227–6234. https://doi.org/10.1021/acs.nanolett.5c00791.
12. Yang, T., Jiang, X., Sun, X., Dong, Y., and Zhu, Y. (2026). Halogen-bond-induced directional electron flow boosts C–C coupling on copper clusters for efficient CO_2 photoreduction to C_2H_6. Appl. Catal. B Environ. Energy *389*, 126572. https://doi.org/10.1016/j.apcatb.2026.126572.
13. Loumissi, T., Ishii, R., Hara, K., Oyumi, T., Abe, I., Li, C., Zhang, H., Hirayama, R., Niki, K., Itoi, T., and Izumi, Y. (2024). Exchange of CO_2 with CO as reactant switches selectivity in photoreduction on Co–ZrO_2 from C_{1-3} paraffins to small olefins. Angew. Chem. Int. Ed. *63*, e202412090. https://doi.org/10.1002/anie.202412090.
14. Ni, B., Zhang, G., Wang, H., Min, Y., Jiang, K., and Li, H. (2023). Correlating oxidation state and surface ligand motifs with the selectivity of CO_2 photoreduction to C_2 products. Angew. Chem. Int. Ed. *62*, e202215574. https://doi.org/10.1002/anie.202215574.
15. Yan, K., Wu, D., Wang, T., Chen, C., Liu, S., Hu, Y., Gao, C., Chen, H., and Li, B. (2023). Highly selective ethylene production from solar-driven CO_2 reduction on the Bi_2S_3@In_2S_3 catalyst with In–S_V–Bi active sites. ACS Catal. *13*, 2302–2312. https://doi.org/10.1021/acscatal.2c05741.
16. Wang, T., Chen, L., Chen, C., Huang, M., Huang, Y., Liu, S., and Li, B. (2022). Engineering catalytic interfaces in $Cu^{\delta+}$/CeO_2–TiO_2 photocatalysts for synergistically boosting CO_2 reduction to ethylene. ACS Nano *16*, 2306–2318. https://doi.org/10.1021/acsnano.1c08505.
17. Liu, S., Chen, X., Yu, J., Li, N., and Zhou, Q. (2025). Interfacial synergy between Cu nanoclusters and oxygen vacancies on CeO_2 for enhanced selective photoreduction of CO_2 to C_2H_4. J. Mater. Chem. A *13*, 30095–30107. https://doi.org/10.1039/d5ta05362e.
18. Chen, K.-X., Wang, Y., Dong, Y.-Q., Zhao, Z.-H., Zang, Y., Zhang, G.-L., Liu, Y., and Zhang, F.-M. (2025). Theoretical design of dual-site metallocovalent organic frameworks for efficient CO_2 photoreduction into C_2H_4. Appl. Catal. B Environ. Energy *365*, 124933. https://doi.org/10.1016/j.apcatb.2024.124933.
19. Wu, Y., Jiang, J., Chen, Q., Zhu, C., Yu, D., Lu, N., and Mao, J. (2026). Synergistic Interplay of Ni Single Atoms and Neighboring Mn_2 Dual Atoms Enabling Selective Photocatalytic Reduction of CO_2 to Propane. Angew. Chem. Int. Ed. *65*, e21193. https://doi.org/10.1002/anie.202521193.
20. Chakraborty, S., Das, R., Riyaz, M., Das, K., Singh, A.K., Bagchi, D., Vinod, C.P., and Peter, S.C. (2023). Wurtzite $CuGaS_2$ with an in-situ-formed CuO layer photocatalyzes CO_2 conversion to ethylene with high selectivity. Angew. Chem. Int. Ed. *62*, e202216613. https://doi.org/10.1002/anie.202216613.
21. Das, R., Paul, R., Parui, A., Shrotri, A., Atzori, C., Lomachenko, K.A., Singh, A.K., Mondal, J., and Peter, S.C. (2023). Engineering the charge density on an $In_{2.77}S_4$/porous organic polymer hybrid photocatalyst for CO_2-to-ethylene conversion reaction. J. Am. Chem. Soc. *145*, 422–435. https://doi.org/10.1021/jacs.2c10351.

22. Zhang, Z., Hu, Q., Xie, J., Yan, W., Hu, J., Zhu, J., Pan, Y., Liu, W., Liu, H., and Jiao, X. (2025). CO_2 Photoreduction into C_2 Fuels Steered by Heteroatom Pair Sites in M_xO_y@Bi_2S_3 Heterojunction. ACS Catal. *15*, 14021–14028. https://doi.org/10.1021/acscatal.5c04257.

23. Wang, S., Nie, X., Song, C., and Guo, X. (2024). Computational identification of high-efficiency dual-metal-atom-modified Ti-metal–organic frameworks for photocatalytic CO_2 reduction to value-added chemicals. CCS Chem. *6*, 3018–3029. https://doi.org/10.31635/ccschem.024.202404583.

24. Xia, X.-C., Cheng, F., Sun, P., Dubale, A.A., Han, H., Cui, E.-T., Song, J., Yang, X.-L., and Xie, M.-H. (2024). Versatile MOF-based nanofibrous heterostructures for engineering the CO_2photoreduction activity and selectivity: from CO to C_2H_5OH. Chem. Eng. J. *491*, 152096. https://doi.org/10.1016/j.cej.2024.152096.

25. Liu, Z., Mao, L., Liu, Z., Zhou, M., Wang, H., Li, J., Zhang, R., Nie, K., Yan, B., Zhang, H., et al. (2026). Ethanol synthesis by CO_2 photoreduction catalyzed by self-optimized $Ti^{\delta+}$-based heterojunction. Angew. Chem. Int. Ed. *65*, e22838. https://doi.org/10.1002/anie.202522838.

26. Xue, F., Zhang, C., Liu, M., Liu, F., Yan, X., Liu, S., Peng, H., Hu, Z., Pao, C.-W., Huang, W.-H., et al. (2025). CO_2-to-C_2H_5OH photoconversion by an amorphization-activated catalyst. Chem Catal. *5*, 101293. https://doi.org/10.1016/j.checat.2025.101293.

27. Tan, H., Si, W., Zhang, R., Peng, W., Liu, X., Zheng, X., Hou, F., Yin, L., and Liang, J. (2025). Dual active sites with charge-asymmetry in organic semiconductors promoting C−C coupling for highly efficient CO_2 photoreduction to ethanol. Angew. Chem. Int. Ed. *64*, e202416684. https://doi.org/10.1002/anie.202416684.

28. Sun, F.-L., Lin, C.-b., Luo, Z.-r., Chen, Q., Chen, W.-X., and Zhuang, G.-L. (2025). Multichannel photon simulated C−C coupling for CO_2 reduction in a mixed water/acetonitrile solvent. Angew. Chem. Int. Ed. *64*, e202500270. https://doi.org/10.1002/anie.202500270.

29. Chang, X., Wang, T., Zhao, Z.-J., Yang, P., Greeley, J., Mu, R., Zhang, G., Gong, Z., Luo, Z., Chen, J., et al. (2018). Tuning Cu/Cu_2O intrerfaces for the reduction of carbon dioxide to methanol in aqueous solutions. Angew. Chem. Int. Ed. *57*, 15415–15419. https://doi.org/10.1002/anie.201805256.

30. Zhang, H., Itoi, T., Konishi, T., and Izumi, Y. (2019). Dual photocatalytic roles of light: charge separation at the band gap and heat via localized surface plasmon resonance to convert CO_2 into CO over silver–zirconium oxide. J. Am. Chem. Soc. *141*, 6292–6301. https://doi.org/10.1021/jacs.8b13894.

31. Kovačič, Ž., Likozar, B., and Huš, M. (2020). Photocatalytic CO_2 reduction: a review of ab initio mechanism, kinetics, and multiscale modeling simulations. ACS Catal. *10*, 14984–15007. https://doi.org/10.1021/acscatal.0c02557.

32. Francesco, A., Julia, W., and Alfredo, P. (2018). pH-Dependent catalytic reaction pathway for water splitting at the $BiVO_4$–water interface from the band alignment. ACS Energy Lett. *3*, 829–834.

33. Francesco, A., Julia, W., and Alfredo, P. (2018). pH-Dependent surface chemistry from first principles: application to the $BiVO_4$ (0 1 0)–water interface. ACS Appl. Mater. Interfaces *10*, 10011–10021.

34. Ou, L., and He, Z. (2020). Potential-dependent competitive electroreduction of CO_2 into CO and formate on Cu (1 1 1) from an improved H coverage-dependent electrochemical model with explicit solvent effect. ACS Omega *5*, 12735–12744. https://doi.org/10.1021/acsomega.0c00227.

35. Iqbal, A., Tripathi, A., and Thapa, R. (2024). C_2 product formation over the C_1 product and HER on the 1 1 1 plane of specific Cu alloy nanoparticles identified through multiparameter optimization. Inorg. Chem. *63*, 1462–1470. https://doi.org/10.1021/acs.inorgchem.3c03984.

36. Nitopi, S., Bertheussen, E., Scott, S.B., Liu, X., Engstfeld, A.K., Horch, S., Seger, B., Stephens, I.E.L., Chan, K., Hahn, C., et al. (2019). Progress and perspectives of electrochemical CO_2 reduction on copper in aqueous electrolyte. Chem. Rev. *119*, 7610–7672. https://doi.org/10.1021/acs.chemrev.8b00705.

37. Henkelman, G., Uberuaga, B.P., and Jónsson, H. (2000). A climbing image nudged elastic band method for finding saddle points and minimum energy paths. J. Chem. Phys. *113*, 9901–9904. https://doi.org/10.1063/1.1329672.

38. Ásgeirsson, V., Birgisson, B.O., Bjornsson, R., Becker, U., Neese, F., Riplinger, C., and Jónsson, H. (2021). Nudged elastic band method for molecular reactions using energy weighted springs combined with eigenvector following. J. Chem. Theor. Comput. *17*, 4929–4945. https://doi.org/10.1021/acs.jctc.1c00462.

39. Henkelman, G., and Jónsson, H. (1999). A dimer method for finding saddle points on high dimensional potential surfaces using only first derivatives. J. Chem. Phys. *111*, 7010–7022. https://doi.org/10.1063/1.480097.

40. Jay, A., Gunde, M., Salles, N., Poberžnik, M., Martin-Samos, L., Richard, N., Gironcoli, S.d., Mousseau, N., and Hémeryck, A. (2022). Activation–relaxation technique: an efficient way to find minima and saddle points of potential energy surfaces. Comput. Mater. Sci. *209*, 111363. https://doi.org/10.1016/j.commatsci.2022.111363.

41. Wang, M., Jia, J., Xia, J., Peng, C.K., He, J., Qiu, Y., He, Y., Gao, L., Xue, F., Lin, Y.G., et al. (2025). CO_2 hydrogenation to HCOOH catalyzed by aqueous Pd needle assembly. Nat. Commun. *16*, 6454. https://doi.org/10.1038/s41467-025-61747-5.

42. Jeffrey, R.D.L., and Normand, M. (2023). Diffusion of oxygen formed at the anatase (1 0 1) surface: an activation-relaxation technique study. Phys. Rev. Mater. *7*, 034602.

43. Jisu, J., Hyungmin, A., and Seungwu, H. (2024). Modified activation–relaxation technique (ARTn) method tuned for efficient identification of transition states in surface reactions. J. Chem. Theor. Comput. *20*, 8024–8034.

44. Barducci, A., Bussi, G., and Parrinello, M. (2008). Well-tempered metadynamics: a smoothly converging and tunable free-energy method. Phys. Rev. Lett. *100*, 020603. https://doi.org/10.1103/PhysRevLett.100.020603.

45. Reuter, K., Frenkel, D., and Scheffler, M. (2004). The steady state of heterogeneous catalysis, studied by first-principles statistical mechanics. Phys. Rev. Lett. *93*, 116105. https://doi.org/10.1103/PhysRevLett.93.116105.

46. Saleem, U., and Sharada, S.M. (2026). Impact of surface vacancies on the dynamics of metal atoms on reducible oxides: an enhanced sampling study with machine-learned potentials for Pt_1/TiO_2. J. Mater. Chem. A *14*, 12362–12380. https://doi.org/10.1039/d5ta09561a.